Titre: Title:	A Novel CMOS Micro-Spectrometer Based on Wavelength Absorption
Auteur: Author:	Kai Zhang
Date:	2017
Type:	Mémoire ou thèse / Dissertation or Thesis
Référence: Citation:	Zhang, K. (2017). A Novel CMOS Micro-Spectrometer Based on Wavelength Absorption [Mémoire de maîtrise, École Polytechnique de Montréal]. PolyPublie. https://publications.polymtl.ca/2758/

URL de PolyPublie: PolyPublie URL:	https://publications.polymtl.ca/2758/
Directeurs de recherche: Advisors:	Yves Audet
Programme: Program:	génie électrique

UNIVERSITÉ DE MONTRÉAL

A NOVEL CMOS MICRO-SPECTROMETER BASED ON WAVELENGTH ABSORPTION

KAI ZHANG
DÉPARTEMENT DE GÉNIE ÉLECTRIQUE
ÉCOLE POLYTECHNIQUE DE MONTRÉAL

MÉMOIRE PRÉSENTÉ EN VUE DE L'OBTENTION
DU DIPLÔME DE MAÎTRISE ÈS SCIENCES APPLIQUÉES
(GÉNIE ÉLECTRIQUE)
AOÛT 2017

UNIVERSITÉ DE MONTRÉAL

ÉCOLE POLYTECHNIQUE DE MONTRÉAL

Ce mémoire intitulé:

A NOVEL CMOS MICRO-SPECTROMETER BASED ON WAVELENGTH ABSORPTION

présenté par: ZHANG Kai

en vue de l'obtention du diplôme de : Maîtrise ès Sciences Appliquées

a été dûment accepté par le jury d'examen constitué de :

M. SAVARIA Yvon, Ph. D., président

M. AUDET Yves, Ph. D., membre et directeur de recherche

M. SIROIS Frédéric, Ph. D., membre

DEDICATION

To my parents, who love me and support me all the time.

To my father, may you rest in peace.

ACKNOWLEDGEMENTS

In the past years, I struggled and fought for my project. After countless failures, dawn finally comes. I would like to take the hard-earned opportunity to thank various people who helped me to complete this achievement.

First of all, I would like to express my deep gratitude and appreciation to my research supervisor, Prof. Yves Audet, for providing continued support throughout my entire program. Thanks to his profound knowledge in semiconductor device and electric circuits, as well as his great patience at all times. The memory of many nights, we discussed the problems until midnight, is precious and unforgettable. Without his generous help and wise guidance, I would not have finished my thesis.

I must thank the past and current colleagues in *Groupe de Recherche en Microélectronique et Microsystèms* at Polytechnique Montréal, Jacques Girardin, Réjean Lepage, Jean Bouchard, Bryan Tremblay, and especially Pascal Burasa, whose excellent work provides me a solid basis to develop the spectrometer.

I sincerely acknowledge China Scholarship Council, for offering me three-year scholarship, and giving me the opportunity to study in Canada.

I will thank all my friends, who helped me to survive in the most difficult time.

At the end, I'd like to devote this work to my parents. My father passed away because of cancer in 2010 while I was studying in Canada. My mother took care of my father and shouldered all family burden by herself during those years. No words could express how much love and appreciation to them.

RÉSUMÉ

L'analyse spectrométrique est une technique largement utilisée pour étudier les matériaux et les composés. Les spectromètres modernes dédiés à la recherche sont des instruments encombrants composés d'une source lumineuse, d'un élément de dispersion, de lentilles, d'un capteur photonique, de composants électromécaniques et de circuits électroniques de contrôle, de traitement de données et de mémoire. Les éléments de dispersion les plus couramment employés sont les prismes et les réseaux de diffraction ou d'interférence. Les éléments de dispersion sont irremplaçables dans les spectromètres modernes.

Dans cette thèse, une nouvelle méthode pour la détection du spectre basée sur l'absorption des photons dans le Silicium, matériau de base employé dans les procédés de fabrication microélectronique, est proposée. Le spectromètre, nommé Wavelength Absorption Spectrometer (WAS), n'utilise aucun élément de dispersion. Les technologies de fabrication CMOS permettent d'implémenter sur la même puce, le détecteur et les composants de traitement de signal du spectromètre.

La profondeur de pénétration de la lumière incidente dépend de la longueur d'onde pour un matériau semi-conducteur spécifique de sorte que l'information spectrale peut être obtenue en mesurant la concentration en excès de paires électron-trou photo générés en fonction de la profondeur. Le transport des charges en excès photo-générées dépend de la concentration des dopants, de la distribution des champs électrique et magnétique, du taux de génération et de recombinaison, de la vitesse de recombinaison de surface, de la durée de vie des charges, de la température et de la géométrie du dispositif.

La thèse traite en détail le principe de détection proposé et présente les résultats expérimentaux d'un prototype WAS. Trois longueurs d'onde, 470 nm, 530 nm et 640 nm, avec plusieurs irradiances, sont utilisées afin de vérifier le principe de détection utilisant un champ magnétique externe. Lorsque la concentration du transporteur est élevée, les résultats expérimentaux confirment l'analyse théorique que la longueur d'onde devient indiscernable, car le mécanisme de recombinaison Auger est dominant. Un modèle d'éléments finis confirme le principe de détection des trous en excès en fonction de la profondeur où la trajectoire des trous en mouvement est déviée sous la force de Lorentz vers un ensemble de collecteurs. Afin de réaliser le spectromètre, une méthode de détection du spectre lumineux est développée, ce qui nécessite un ensemble d'équations linéaires où les coefficients de la matrice proviennent de la mesure de la densité de courant en fonction de l'irradiance pour différentes longueurs d'ondes et champs magnétiques.

Différent du spectromètre traditionnel, la résolution de WAS dépend des courants détectables minimaux de trou. Le calcul théorique prédit que la résolution du WAS se situe au environ de 219 selon le niveau de bruit provenant des jonctions de collecteurs.

Afin de développer un spectromètre plus compact et peu coûteux, deux prototypes sont modélisés où le principe de détection ne requiert aucune génération de champ magnétique. Cependant, la faible résolution est un inconvénient principal de ces structures modifiées.

ABSTRACT

Spectrometry analysis is a widely used technique to investigate materials and structures. The current research-grade spectrometers are bulky equipment composed of a light source, a dispersing element, lenses, an optical sensor, electromechanical components and an electronic circuit. The commonly used dispersing elements mainly include a prism, diffraction grating, or an interference component. The dispersing elements are irreplaceable in modern spectrometers.

In this thesis, a novel method of detecting the spectrum based on wavelength absorption phenomenon in silicon is proposed; it is called Wavelength Absorption Spectrometer (WAS). CMOS integrated circuit technology is highly mature and allows the detector and the signal processing component to be implemented on the same chip.

The light incident depth depends on its wavelength for a specific semiconductor material, thus the wavelength spectral information is obtained by measuring the photo-generated electron-hole pairs as a function of depth. Under the electric and magnetic field, the photo-generated holes are collected by reverse-biased PN junctions. The excess carrier transportation depends on the doping concentration, the electric and magnetic field distribution, the generation-recombination rate, the surface recombination velocity, carriers' life time, the temperature, and the device geometry. All of these factors are discussed in the thesis.

The thesis discusses the proposed detection principle in detail and presents experimental results of a WAS prototype. Three wavelengths, 470 nm, 530 nm and 640 nm, with several irradiances, are used to test the prototype under a varying external magnetic field. When the carrier concentration is high, experimental results confirm the theoretical analysis that wavelength becomes indistinguishable because the Auger recombination mechanism is dominant. A finite element model confirms the excess holes’ detection principle as a function of depth where moving holes’ trajectory is deviated under the Lorentz force towards a set of collectors. In order to realize a spectrometer, a light spectrum detection method is developed, which requires a linear equation set where coefficients of the matrix come from the measurement of the current density as a function of the irradiance for different wavelengths and magnetic fields.

Different from the traditional spectrometer, the resolution of WAS depends on the minimal detectable current of excess holes. The theoretical calculation predicts that the resolution of the WAS could reach around 219 depending on the collectors’ junction shot noise.

In order to develop a more compact spectrometer, two models are conceived where the detection principle does not rely on space-consuming magnets. However, the low resolution is the main disadvantage of these modified structures.

TABLE OF CONTENTS

LIST OF FIGURES

LIST OF SYMBOLS AND ABBREVIATIONS

CCD	Charge-Coupled Device
COMSOL^{TM}	A multi-physics finite element method software
CMOS	Complementary Metal-Oxide-Semiconductor
ELF	Extremely Low Frequency
FEM	Finite Element Method
FWHM	Full Width at Half Maximum
MATLAB	Matrix Laboratory, a numerical computing software
MOSFET	Metal-Oxide Semiconductor Field-Effect Transistor
NMOS	N-channel MOSFET
NMR	Nuclear Magnetic Resonance
PMOS	P-channel MOSFET
SRH	Shockley-Read-Hall recombination
TFD	Transverse Field Detector
VHDL	VHSIC Hardware Description Language
VHSIC	Very High Speed Integrated Circuit
WAS	Wavelength Absorption Spectrometer

LIST OF APPENDICES

CHAPTER 1 INTRODUCTION

1.1 General Background

Spectrometry analysis is a widely used technique to investigate materials and structures. The current research-grade spectrometers are bulky equipment composed by a light source, a dispersing element, lenses, an optical sensor, electromechanical components and an electronic circuit [1]–[5]. The commonly used dispersing elements can be categorized in three main groups according to the mechanism involved in the extraction of spectral information from optical signals: spatial dispersion, interferometer, and resonance. The dispersing element determines the resolution of a spectrometer. A Charge-Coupled Device (CCD) [6], [7] or Active Pixel Sensor (APS) [8]–[16] detects the signals behind the dispersing elements.

Solid-state physics have demonstrated that photons penetrating into semiconductor material interact with atoms, and generate electron-hole pairs. This process is called photon absorption. A measure of the intensity reduction of the photon flux is the absorption coefficient, and it is function of wavelengths. This characteristic has been employed to fabricate color sensors without filters [17], however, the filter-less optical spectrometer area is a virgin land to be discovered.

Enlighted from this concept, a novel filter-less spectrum detection method is proposed in this thesis. The method enables compact and cost effective spectrometer solutions for a wide range of applications. Using silicon based fabrication processes has the main advantage of having a detector compatible with some advance bipolar or CMOS integrated circuit fabrication processes, meaning that the detector, signal conditioning circuits, and digital processing can be implemented on the same substrate.

1.2 Objectives of the Project

To realize the spectrometer based on the wavelength absorption principle, several objectives should be met.

a) The photo-generated excess carriers' concentration is a function of photon flux intensity, absorption depth, and absorption coefficient for a specific medium. The absorption coefficient is a function of the wavelength. Therefore, the wavelength information can be obtained by measuring the photo-generated electron-hole concentration as a function of depth, at a constant photon flux intensity. For the first objective, we derive the expression of the functions from the continuity equation.

b) To validate the theoretical analysis in step a), we tested a prototype with a magnetic field that enables to detect the carrier concentration along the depth. Finite element method simulations by COMSOL^{TM} validate the Hall Effect as described in step a).

c) The spectrometer is developed based on the proved principle. To realize a spectrometer, both wavelength and irradiance information are necessary. A spectrum detection method is developed to satisfy the requirement.

d) Resolution is a measure of detection ability of a spectrometer, and it is defined as the ratio of wavelength and the resolving power which is the minimal wavelength difference that can be distinguished. We derive the ultimate resolution of the design. Our goal is to have a detection range covering 400 *n*m to 750 *n*m, with a resolution aiming at 100.

1.3 Contributions of the Thesis

By reaching the thesis objectives, the following main contributions will be achieved:

a) The filter-less spectrum detection method is proposed [18] and developed theoretically. The effect of generation-recombination process, Hall Effect, Lorentz force, excess carrier life time, diffusion and drift current, surface recombination velocity, etc., are included in the calculations.

b) Non-linear differential equations can't be solved analytically, hence multi-physics finite element method software COMSOL^{TM} is used to simulate the photo-generated carriers' generation-recombination and transportation process. Combined with theoretical analysis and COMSOL^{TM} simulations, the proposed idea has been validated with experimental results obtained from a colleague experimental work.

c) The proposed detection principle relies on space-consuming magnets. New designs which eliminate the need of a magnetic field to realize a spectrometer will be discussed.

1.4 Structure of the thesis

The thesis is composed of the following chapters: Chapter 1 introduces a brief background and general information about the project, main contributions, and the structure. Chapter 2 gives an overview of the art of spectrometry, and research status on filter-less color sensors. Chapter 3 presents an article, *A Novel CMOS Spectrometer without Dispersing Elements*, submitted to *SENSORS AND ACTUATORS A,* which presents theoretical and experimental data, validating the feasibility of a spectrometer without any dispersing elements. Chapter 4 discusses the resolution of the proposed spectrometer. Chapter 5 calculates the continuity equations and the effect of important parameters, such as boundary conditions, surface recombination velocity, and carrier lifetime. Chapter 6 demonstrates the procedure to set up a Finite Element Method model, followed by the discussion on two improved compact spectrometer designs that eliminate the need of an external magnetic field. As a conclusion, Chapter 7 summarizes the contributions of the thesis, addresses the limitations, and provides suggestions for future researchers.

All necessary information about the spectrometer, including MATLAB codes, VHDL codes, … etc., will be presented in the Appendix section.

CHAPTER 2 LITERATURE REVIEW

2.1 Optical Absorption

Optical absorption is a process where incident photons with energy larger than the band gap of a semiconductor material are absorbed, and generate electron-hole pairs which are called photo-generated excess carriers.

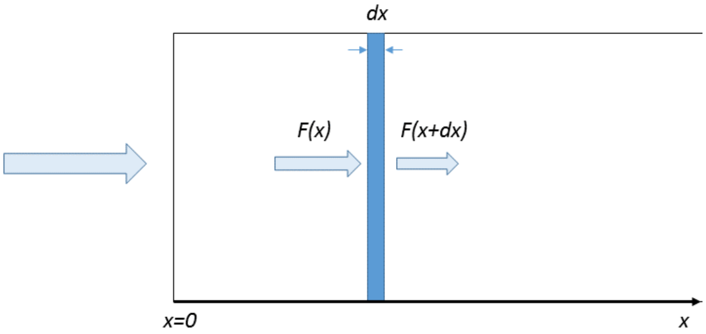

Figure 2-1 Absorption of photon flux in silicon.

For a photon flux *F(x)* penetrating into silicon, as shown in Figure 2-1, a measure of the intensity reduction of photon flux is the absorption coefficient, α [19],

$$\frac{d}{dx}F(x) = \alpha F(x) \tag{2.1}$$

where *x* is the depth of penetration. The solution to Equation (2.1) is

$$F(x) = F_0 e^{-\alpha x} \tag{2.2}$$

where F_0 is the photon flux at the surface (x=0).

The absorption coefficient is a function of the wavelength and depends on semiconductor materials as well. For silicon, the relationship between the absorption coefficient and wavelengths is drawn in Figure 2-2.

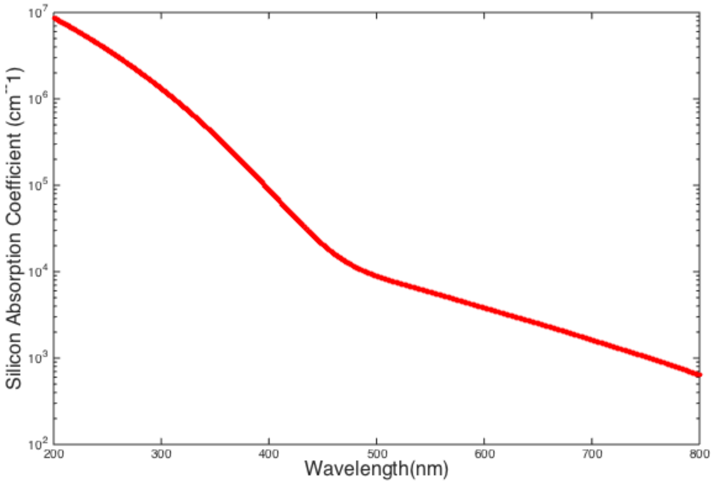

Figure 2-2 Absorption coefficient vs wavelength in silicon.

2.2 Generation and Recombination

A photon with an energy, *hv*, which is larger than the band gap of silicon will excite an electron from the valence band to the conduction band and leave a hole in the valence band. This process is called generation. The typical band gap of silicon is 1.12eV, therefore, the minimum energy to generate electron-hole pair is 1.12eV, corresponding to the maximum photon wavelength of 1.1μm.

The recombination mechanism is the inverse process of the generation. When a free electron is captured by a positive ion, it combines with a hole. The SRH recombination mechanism is active where there are impurities or defects in the semiconductor material and the SRH lifetime is independent of excess carrier density. While Auger lifetime is independent of the impurity and defect densities, it is, however, a function of carrier concentration. In silicon, the Auger recombination mechanism dominates when either the doping density or the excess carrier concentration is very high, and the SRH recombination mechanism prevails at lower concentration [20].

2.3 CCD and CMOS Detector

Detectors are used to record the dispersed monochromatic beams and transform them into electrical signals. Two dominant optical sensor technologies are CCD (Charge-Coupled Device)

[6], [7] and APS (Active Pixel Sensor) [7]. There are several types of APS sensors, and the most widely used type in cell phone cameras, web cameras, and digital single-lens reflex cameras (DSLRs) is produced in CMOS (Complementary Metal-Oxide-Semiconductor) technology, hence, APS sensor is usually known as CMOS sensor.

CMOS image sensors appeared in the 1960s, earlier than CCD sensors. However, CCD sensors were dominant in this field until the 2000s, because of their lower noise, lower dark current, smaller pixel size, 100% fill factor, electronic shutter without artifacts and higher sensitivity [9]. Coming into the new millennium, thanks to the CMOS process state-of-art, CMOS image sensors attracted lots of attention for potentially higher performance than CCD sensors because they can offer many advantages compared to CCD sensors, such as faster response, lower cost, lower power consumption, lower operation voltage, on-chip functionality [9][10], and most importantly, the compatibility with mature CMOS technologies. This allows CMOS sensors to enter production during a very short period with high quality and low cost.

Both CCD and CMOS sensor have large detection bandwidth, covering the visible spectrum, therefore, they have no color selectivity. The color filters are employed on top of the sensor pixels to add color selectivity.

2.4 Hall Effect

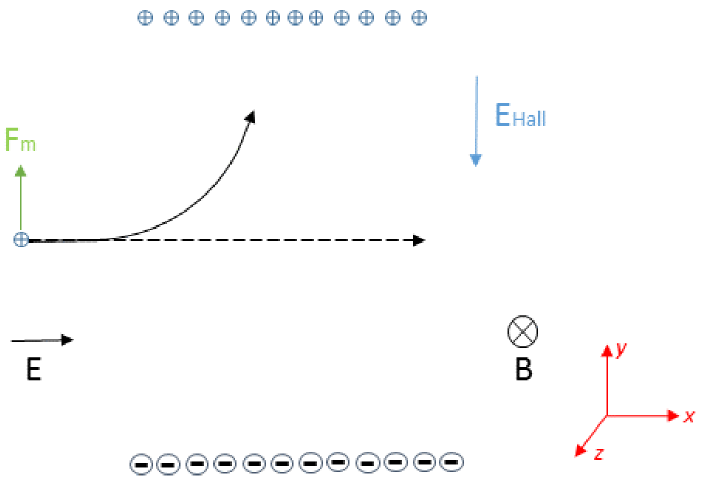

Figure 2-3 The schematic figure of Hall Effect and Lorentz force in a semiconductor.

As illustrated in Figure 2-3, a positive carrier q is moving under the electric field $\boldsymbol{E}$ with the velocity $\boldsymbol{v}$ in the +*x* direction as the dashed line showed. After applying an external uniform magnetic field $\boldsymbol{B}$ along –*z* direction, the carrier will deviate towards to the +*y* direction as the solid curve indicated under the Lorenz force, which is expressed as:

$$\boldsymbol{F}_m = q\boldsymbol{v} \times \boldsymbol{B} \tag{2.3}$$

Thus positive carriers accumulate on top face in silicon and will leave equal negative carriers on the bottom face. The separated charges generate an electric field $\mathbf{E}_{\mathrm{Hall}}$ along the –*y* direction. $\mathbf{E}_{\mathrm{Hall}}$ can be derived when the total force applied on the carrier along the *y* direction equals to 0:

$$\boldsymbol{F} = q[\boldsymbol{E}_{\mathrm{Hall}} + \boldsymbol{v} \times \boldsymbol{B}] = 0 \tag{2.4}$$

$$\boldsymbol{E}_{\mathrm{Hall}} = -\boldsymbol{v} \times \boldsymbol{B} \tag{2.5}$$

2.5 State of the Art in Spectrometry

The electromagnetic spectrum, usually known as the spectrum, is a scientific collective term for all electromagnetic radiation’s frequencies and their linked wavelengths. It covers from gamma radiation to Extremely Low Frequency (ELF) region. Correspondingly, there are many types of spectrometry to measure different spectrum regions, such as X-ray Diffraction Crystallography, Ultraviolet-Visible Spectrometry, Fluorescence Spectrometry, Nuclear Magnetic Resonance (NMR) Spectrometry, Optical Spectrometry, Infrared Spectrometry, etc. [2], [4], [23].

The current research-grade optical spectrometers are bulky equipment composed of a light source, a dispersing element, lenses, an optical sensor, electromechanical components and electronic circuitry. The optical sensor and dispersing elements are the crucial components that determine the detection ability of a spectrometer.

The commonly used dispersing elements can be categorized into three main groups according to the mechanism involved in the extraction of spectral information from optical signals: spatial dispersion, interferometry, and resonance.

The spatial dispersing element mainly includes prism and diffraction grating. The dispersion of the prism is known since the 17th century, and the light obeys the Snell's law at every optical surface. Figure 2-4 shows how a prism disperses an incident light.

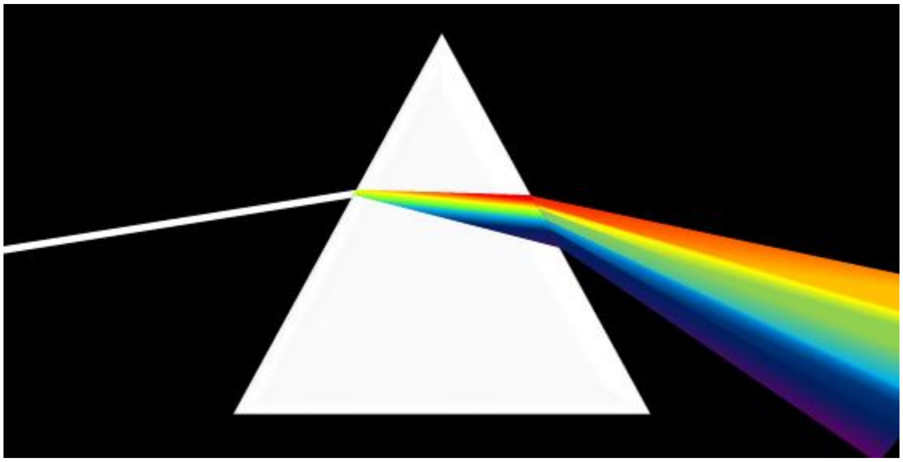

Figure 2-4 Light is dispersed by a prism.

The diffraction grating consists of a series of parallel grooves used to separate the incident light into monochrome component wavelengths with different scattering angles. Figure 2-5 shows how a diffraction grating disperses an incident white light. The zero order (central white) represents a direct transmission through the grating. The first-order and second-order rainbows represent the increasing wavelengths from purple to red due to wavelength related diffraction angles. The diffraction order is determined by the grooves' period, and adjacent order of rainbows may overlap, especially for higher orders. By adjusting the grooves' density, it is possible to concentrate the diffracted energy in a particular order for a given range of wavelength.

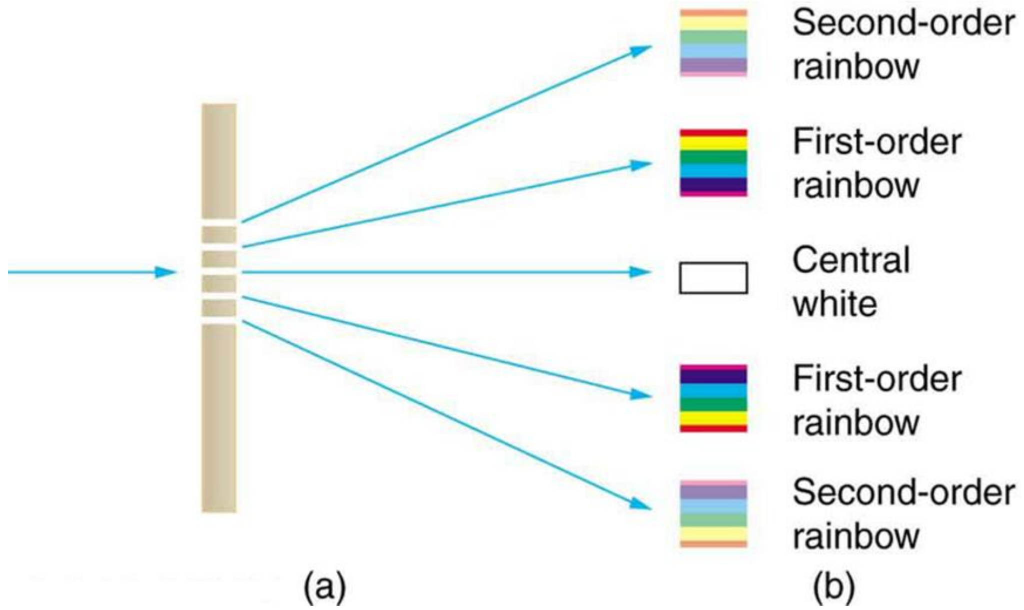

Figure 2-5 Diagram of reflective diffraction grating principle [24].

The interferometer utilizes the interference phenomenon to disperse an incident light and the typical instruments are the Fabry–Pérot interferometer and the Michelson interferometer. They could record the frequency domain spectrum by Fourier transform, so both of them are also known as Fourier transform spectrometers.

As shown in Figure 2-6, a Michelson interferometer is composed of two mirrors M1, M2, a beam splitter M and a detector E. An incident beam produced by coherent light source is split at C by M and reflected by A and B, respectively, and both retuning beams are combined at C' to generate an interference pattern due to the orientation of the mirrors, and the pattern is recorded by the detector E. The optical path difference caused by this process will result in interference. Figure 2-7 illustrates two possible interference fringes. M2' is the image of mirror M2, S1' and S2' are virtual images of source S, respectively. The strictly perpendicular two mirrors M1 and M2 will make S1' and S2' are in line, and will generate fringes of equal inclination (Figure 2-7a), and a slight angle of two mirrors will result in fringes of equal thickness (Figure 2-7b).

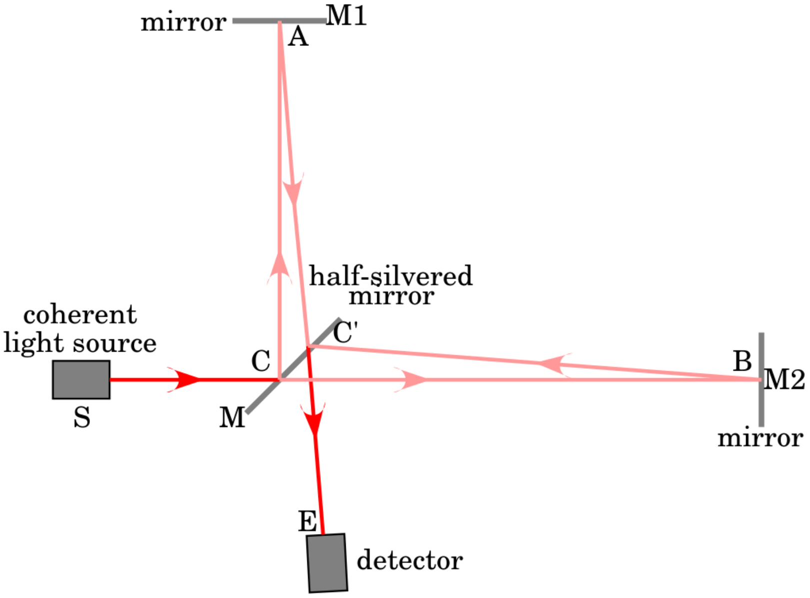

Figure 2-6 Schematic diagram of Michelson interferometer principle [25].

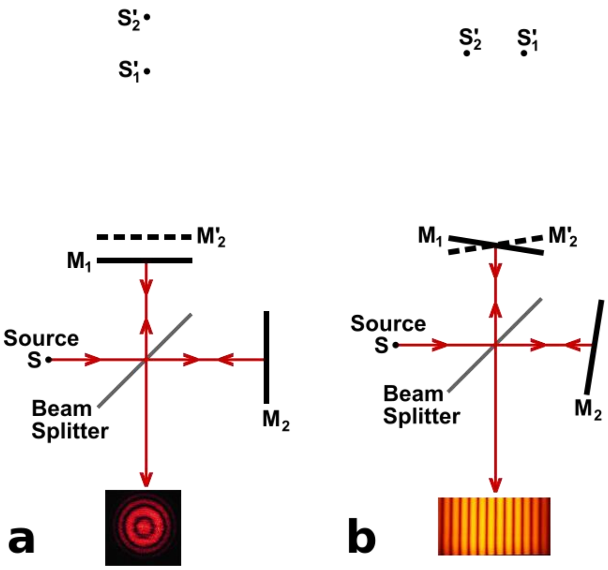

Figure 2-7 Formation of fringes in a Michelson interferometer [26].

S_1' and S_2' represent the mirror images.

2.6 Recent development on filter-less optical sensor

Dispersing elements in a spectrometer are as crucial as color filter in a color sensor, and no one has ever tried to make a spectrometer without them. Giving that both spectrometer and color sensor are optical detection sensors, we present a short review on filter-less optical sensors.

Standard commercial cameras use the Bayer filter pattern [27] adding color sensitivity to CCD and CMOS sensors. However, filters reduce the pixel sensitivity due to the light reflection and scattering, and increase the production cost due to the post-processing filter deposition.

Recently, efforts to make filter-less image sensors have been made. Foveon Incorporated [17][28] has proposed a sensor structure in which three p-n junctions are implanted at different depths as shown in Figure 2-8. The first junction (upper) that is close to the surface collects the carriers generated by all photons in the visible spectrum. The middle junction collects mainly the carriers generated by all photons except the shorter wavelength (blue), and the deepest one collects mainly carriers generated by all photons except the blue and green range of the visible spectrum. The three junctions act as color filters. The latest product based on this detection principle from Foveon Incorporated is a 14.1 megapixels image sensor [29].

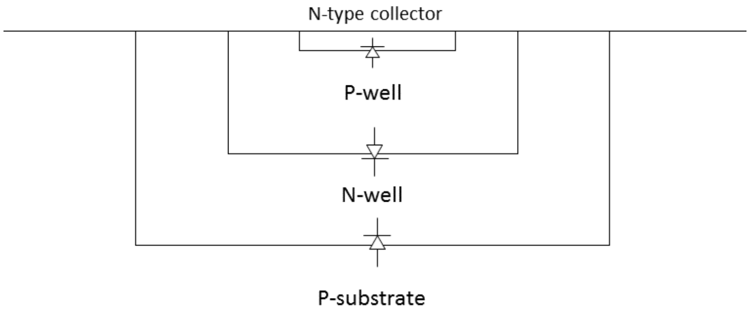

Figure 2-8 Diagram of the Foveon sensor.

Another structure, called Transverse Field Detector (TFD), is proposed by Langfelder et al. in 2009 [30]. They implanted several independent N+ collectors in p-type silicon, applying selective voltages between them to generate an electric field in order to collect the carriers at different depths by different collectors. Figure 2-9 gives the simulation result of an electric field of the

TFD structure. The node n1 collects the carriers above depth X1 which generated by all photons in the visible spectrum, and n2 collects carriers coming from X1 to X2 range where carriers are generated except by blue ones, and n3 collects the all the carriers below depth X2. The three collectors act as color filters.

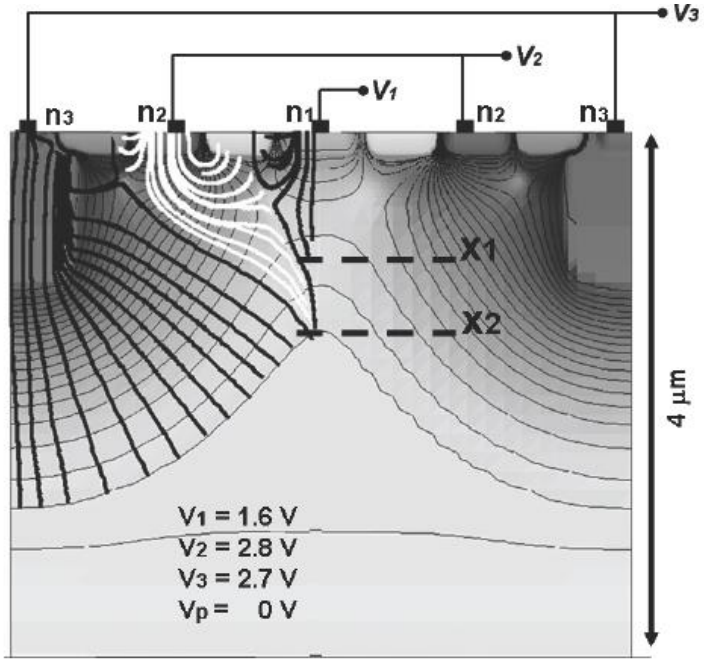

Figure 2-9 TFD simulation result. The streamlines show the electric field. The contact n1 collects the electrons to depth X1, contacts n2 collect electrons to depth X2, and collectors n3 collect other electrons generated in other region. [30] [Year 2009 of original publication].

Maruyama et al. proposed filter-less fluorescence sensor in 2006 [31], and an improved sensor based on the same principle was reported in 2011 [32] by Nakazawa and in 2017 by Tanaka [33]. The structure and principle are given in Figure 2-10 and Figure 2-11, respectively. The voltage of the load transistor VLN is set at 0.5V and n-type substrate VSUB is biased at 5V. RES is the reset signal. The photogate PG has a voltage VG on it, and VG controls the depth where photo-generated carriers can be collected.

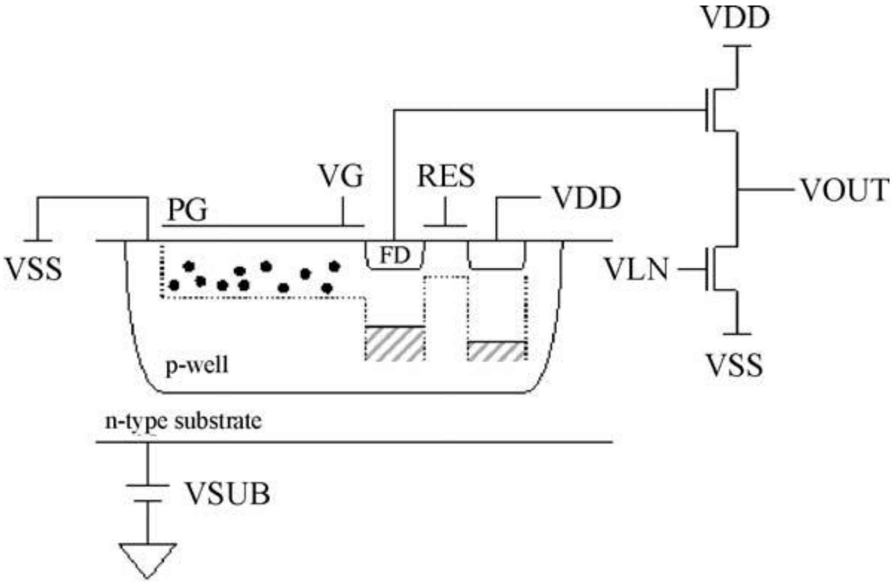

Figure 2-10 Schematic of sensor pixel and readout circuit [31]. Reprinted with permission from Elsevier.

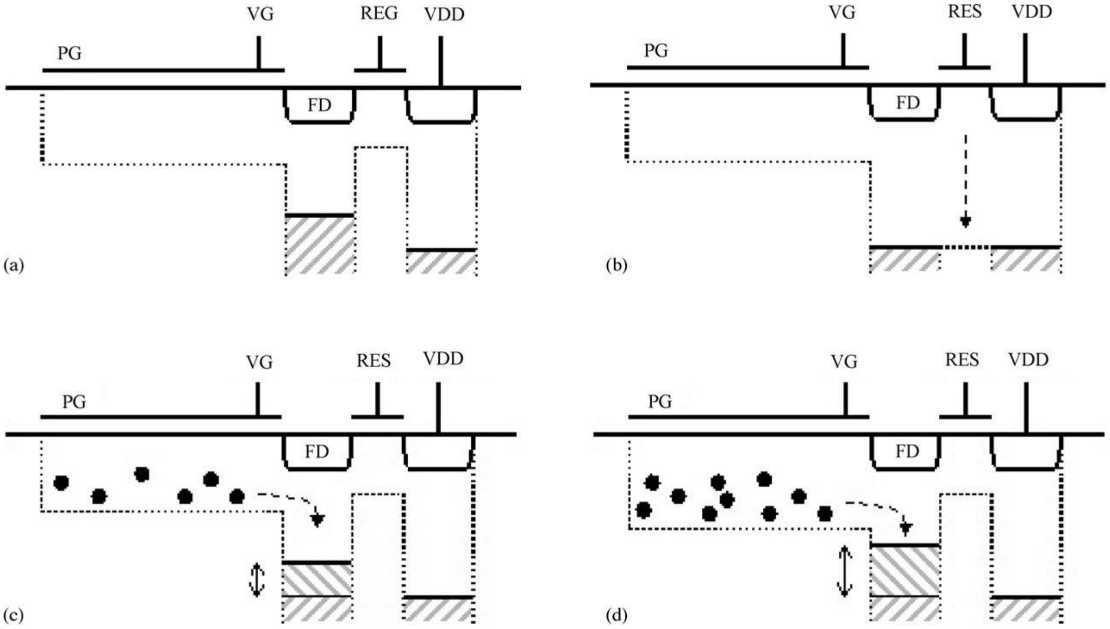

Figure 2-11 Operation of the filter-less fluorescence sensor [31]. Reprinted with permission from Elsevier.

Both VG and RES are set at 0V as in Figure 2-11(a), and RES is set at 5V to reset the floating diffusion (FD) output to 2.5V as shown in Figure 2-11(b). The similar readout operations are indicated in Figure 2-11(c) and (d) with different VG. VG in (d) is larger than in (c) to collect more electrons. The photon generated electrons are accumulated in FD well and the output signal is recorded in voltage after amplification. Because the excitation and fluorescent signals are simultaneous, the intensities could be solved with two VG values at least. Maruyama reported a linear relationship of incident intensity and detected intensity in a wide range of intensities for the fluorescence signal, while the excitation light remains unchanged. As illustrated in Figure 2-12, the author reproduced the excitation and fluorescent lights with 470*n*m and 530*n*m simultaneously, and kept the intensity of the excitation light constant, while varying it for 530*n*m. This relationship characterized the fluorescent wavelength.

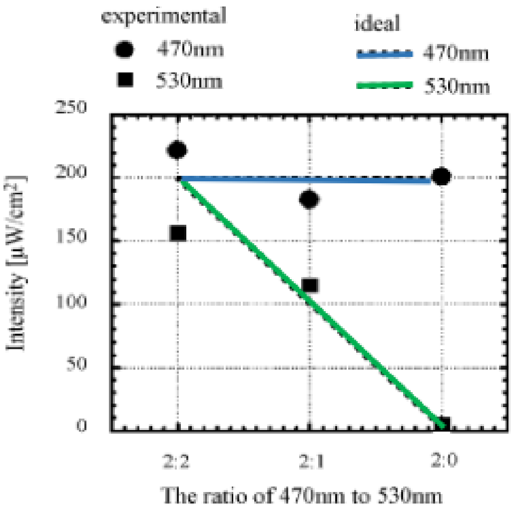

Figure 2-12 Output of the filter-less fluorescence sensor [31]. Reprinted with permission from Elsevier.

The sensor could detect the wavelength based on the linear ratio of fluorescence-to-excitation light since the wavelength and the intensity of the excitation light are already known.

2.7 Miniaturized spectrometer

The current research-grade spectrometer is bulky because it contains components and some space is necessary for an optical path. Some efforts have been made to miniaturized spectrometers and a handful of new products have emerged on the market to provide compact spectrometry solutions ([6], [34]–[43]) Traditional spatial dispersion elements, such as lens and gratings, are still employed. However, exquisite optical path designs allow the spectroscopic systems to be accommodated in small containers.

2.8 Summary

Current spectrometers employ dispersing elements to discriminate the spectrum of an incident light. The widely used dispersing elements in optical spectrometer, including prism, grating, and interferometer are introduced. So far, no effort has been made to fabricate an optical spectrometer without dispersing elements.

Efforts made on the development of filter-less color sensor is a good starting point for the design of spectrometers without dispersing elements. The Foveon's sensor and the TFD could detect three colors (red, green and blue.) It is a great result for color sensitivity but insufficient to distinguish the spectrum. Nakazawa's design is able to detect up to three monochrome wavelengths simultaneously. However, it needs a calibration light signal every time which limits its applications.

At the same time, people have been working on miniaturization of a spectrometer. The efforts mainly focus on minimizing the volume of dispersing element and the optical path in order to reduce space requirement. One of the benefits of removing dispersing elements is that the required space is reduced so that more compact spectrometers can be fabricated

.

CHAPTER 3 A NOVEL CMOS SPECTROMETER BASED ON WAVELENGTH ABSORPTIOION

3.1 Abstract

This article reports on a novel spectrometer without dispersing elements fabricated in standard CMOS technology. The spectrum detection principle is based on the wavelength absorption mechanism in silicon. A finite element model confirms the excess holes' detection principle as a function of depth where moving holes' trajectory is deviated under the Lorentz force towards a set of collectors. In the case of high excess carrier concentration, experimental results confirm the theoretical analysis that wavelength becomes indistinguishable because the Auger recombination mechanism is dominant, which should be avoided to realize a spectrometer. For the low excess carrier concentration case, the concentration profile is determined by the incident irradiance and the wavelength and can be additive since the Shockley-Reed-Hall recombination mechanism prevails, where the excess carrier life time is constant, and hence suitable for wavelength discrimination. In order to realize a spectrometer, a light spectrum detection method is developed, which requires a linear equation set where coefficients of the matrix coming from the measurement of the current density as a function of the irradiance for different wavelengths and magnetic fields. The proposed miniature and integrated spectrometer with a pixel array can be used as a spectral imager.

3.2 Introduction

Spectroscopy analysis is a powerful tool to investigate materials and structures. The current research-grade spectrometers are bulky equipment composed of a dispersing element, lenses, photo-detectors, electromechanical components and electronic circuits. The commonly used dispersing elements can be categorized into three main groups according to the mechanism involved in the extraction of spectral information from optical signals: spatial dispersion, interferometer, and resonance [1]. The latter group encompasses spectrometers using materials having properties of absorption, transmission, and reflection that are dependent on the wavelength. Recently a lot of interest has emerged in employing new structures and new materials such as photonic crystals, metamaterials [44], [45] and quantum dots [1] as the detecting component of a spectrometer. In that respect, a color image sensors design to exploit the wavelength dependent absorption properties of silicon has been developed where the three primary colors employed in digital imaging, blue, green and red are extracted without thin film filtering. Recently, efforts have been made to miniaturized spectrometers and a handful of new products have emerged on the market to provide compact spectrometry solutions[34]–[37]. Traditional spatial dispersion elements, such as lens and gratings, are still employed. However, exquisite optical path designs allow the spectroscopic systems to be accommodated in small containers.

In this paper, we propose a new method of detecting the spectral content of luminous signals by exploiting the absorption properties of semiconductors. The method enables compact and cost effective spectrometer solution for a wide range of applications. Using silicon has the main advantage of having a detector compatible with some advance bipolar or CMOS integrated circuit fabrication processes, meaning that on the same substrate, the detector, signal conditioning circuits and digital processing can be implemented. The proposed principle employs the Lorentz force applied to moving charged particles in the presence of a magnetic field in order to relate wavelengths to the depth of photo-generated carriers. The paper is divided as follows: in Section 3.3, an overview of the underlying physics of carrier generation in semiconductor is described, followed by a description of the carrier concentration profiling method using the Lorentz force; in Section 3.4, a wavelength detection method is developed and also verified experimentally. It relies on a linear system of equations where the coefficients have been obtained from electrical measurement as a function of the optical irradiance for different wavelengths and magnetic fields. Finally, concluding remarks are presented.

3.3 Detection Principle

A monochrome light beam generates a unique excess carrier distribution along the incident depth due to the absorption coefficient. Hence, the wavelength information can be obtained by measuring the photo-generated carrier concentration as a function of depth, and the proposed spectrometer is named the Wavelength Absorption Spectrometer (WAS).

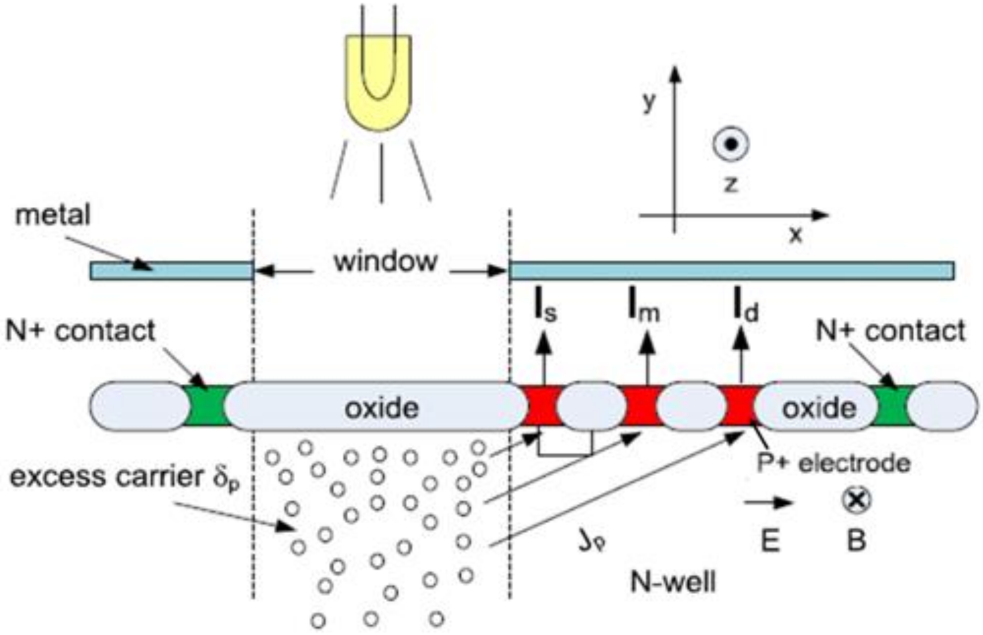

Figure 3-1 The schematic figure of the WAS prototype.

Figure 3-1 illustrates the schematic diagram of a WAS pixel. An N-well region is made in a P-type silicon substrate. Three P+ electrodes (red in Figure 3-1) are heavily doped regions and forms PN junctions with the N-well. The junctions are reversed biased to collect holes only. A uniform electric field along the +*x* direction is produced by the voltage difference between the two N+ contacts. Light penetrates into silicon through a window area and the oxide layer. Other regions are covered by metal to block the illumination. The light-generated electron-hole pairs are separated by the electric field, and electrons move along the -*x* direction and holes move along the +*x* direction. In this first WAS prototype, an external uniform magnetic field is applied along the -*z* direction, thus, the holes' current flows towards the three P+ electrodes due to the Lorenz force. For a specific electric and magnetic field combination, the angle of deflection of holes' current density is constant, so that the electrodes could collect holes from a specific depth. Holes are collected by the middle P+ electrode and form the hole current I_m, while the left and the right P+ electrodes collect holes above and below that specific depth, and form current I_s and I_d, respectively. As a result, excess holes' concentration profile along the depth (-*y* direction) could be achieved by varying the magnetic field, hence, the current density angle of deflection.

In the theoretical analysis, we firstly derive the equation giving the photo-generated excess holes' concentration distribution along the *–y* direction, and secondly, the excess holes' transportation mechanism from the window area to the P+ collectors is validated with a finite element model implemented in the software tool COMSOL^{TM} [46] and experimental result.

3.3.1 The excess holes' generation and recombination

The steady-state continuity equation describes the carrier behavior under the constant incident illumination [47]. Considering the holes' concentration variation along the depth under the window area, the equation becomes

$$\mathrm{D}_p \frac{\mathrm{d}^2\delta_p(|\mathrm{y}|)}{\mathrm{dy}^2} - \frac{\delta_p(|\mathrm{y}|)}{\tau_p} + \mathrm{g}_p = 0 \tag{3.1}$$

where δ_P is the excess holes' concentration, D_p, the diffusion coefficient [48], and, $|y|$, the depth from the surface ($y=0$). For an illumination irradiance, P, at a specific wavelength, λ, the generation rate, g_p, is defined as [20]

$$\mathrm{g}_p = \frac{\mathrm{P}\lambda}{hc}\alpha_\lambda(1 - \mathrm{Re})\mathrm{e}^{-\alpha_\lambda|y|} \tag{3.2}$$

where α_λ is the absorption coefficient, Re is the reflectivity at the Si/SiO$_2$ interface, *h* is Plank constant, and *c* is the speed of light.

The hole recombination lifetime, τ_P, is not constant and is determined by the Auger and the Shockley-Read-Hall (SRH) recombination mechanisms

$$1/\tau_p = 1/\tau_{\mathrm{Auger}} + 1/\tau_{\mathrm{SRH}}\ . \tag{3.3}$$

The SRH recombination mechanism is active where there are impurities or defects in the semiconductor material while Auger lifetime is independent of the impurity and defect densities.

In silicon, the Auger recombination mechanism dominates when either the doping density or the excess carrier concentration is very high, and the SRH recombination mechanism prevails at lower concentration [20]. Auger lifetime is a function of carrier concentration, while SRH lifetime is independent of excess carrier density.

At high concentration in N-type silicon as in the scenario of Figure 3-1, the Auger recombination mechanism dominates and the hole lifetime becomes

$$\tau_p = \tau_{\mathrm{Auger}} = 1/[\mathrm{C}_n(n_0^2 + 2n_0\delta_P + \delta_P^2) + \mathrm{C}_p(p_0^2 + 2p_0\delta_P + \delta_P^2)] \tag{3.4}$$

where C_p and C_n are the Auger recombination coefficients for holes and electrons respectively [11]. For holes' excess concentration δ_P of 10^{20} cm^{-3}, which is much larger than the equilibrium concentration of electrons, n_0, and holes, p_0, Equation (3.4) becomes

$$\tau_p = \tau_{\mathrm{Auger}} = 1/[\delta_P^2(\mathrm{C}_n + \mathrm{C}_p)] \tag{3.5}$$

and the lifetime decreases rapidly to reach approximately 1 ns [20]. In these conditions, the recombination term in Equation (3.1) is dominant and the continuity equation becomes

$$\mathrm{D}_p \frac{\mathrm{d}^2\delta_p(|\mathrm{y}|)}{\mathrm{dy}^2} - \frac{\delta_p(|\mathrm{y}|)}{\tau_p} = 0. \tag{3.6}$$

Consider the boundary conditions $\delta_p(0) = \mathrm{g}_p(0)$, where $\delta_p(0)$ is the surface excess hole density and $\delta_p(\infty) = 0$, the analytical solution of Equation 3-6 is:

$$\frac{1}{\delta_p(\mathrm{y})} = \frac{|y|}{\sqrt{2\mathrm{D}_p/(\mathrm{C}_n+\mathrm{C}_p)}} + \frac{hc}{\mathrm{P}\lambda\alpha_\lambda(1-\mathrm{Re})}\,. \tag{3.7}$$

and reveals that the slope of the reciprocal of photo-generated holes' concentration versus depth is wavelength-independent at high carrier concentration condition. A high incident illumination induces a high carrier concentration, and Equation (3.7) indicates that high illumination must be avoided for the spectrometer application.

At lower photo-generated carrier concentrations, for example, when the concentration can be compared to the equilibrium concentration, both Auger and SRH recombination mechanisms play roles, and g_p can't be ignored in Equation (3.1). g_p is wavelength-dependent, therefore, the carrier concentration distribution along depth provide the spectrum information of the incident light. However, given the relationship of τ_P and g_p , Equation (3.1) is a non-linear non-homogenous differential equation that doesn't have an analytical solution. The effort to reveal the relationship of carrier concentration vs. depth by experiments is reported in Part 3.3.3.

3.3.2 The excess holes' transportation under magnetic field

Analysis of the holes' current density traveling from the volume under the window area up to the collectors and submitted to perpendicular electric and magnetic fields requires coupled equations involving drift and diffusion current densities. Adding to that the geometrical effect of adjacent collectors, makes the derivation of an analytical solution extremely complicated and most likely not representative of the structure. Instead, a Finite Element Method (FEM) model implemented with the multi-physics software tool COMSOL^{TM} is employed to validate the holes' transportation.

Excess electrons and holes are separated and form current densities under the electric and magnetic field. The hole's current density obeys the equation [49]

$$\boldsymbol{J}_p\,(\boldsymbol{B}) = \boldsymbol{J}_p\,(0) + \mu_P\big(\boldsymbol{J}_{\boldsymbol{p}}\,(\boldsymbol{B}) \times \boldsymbol{B}\big) \tag{3.8}$$

where $\boldsymbol{J}_p\,(0)$ is the hole current density without magnetic field, $\boldsymbol{B}$, and it includes drift and diffusion components. Drift current density is a function of electric field and is expressed as $J_{p\_drift}\,(0) = q\mu_P\delta_P E_x$, where q is the elementary charge. Diffusion current density is mainly due to the concentration difference between the illuminated and the shaded area in the substrate.

From the diffusion equation [47], the average diffusion current density is $J_{p\_diff}\,(0) = qD_p\delta_P\left(1 - e^{-L/L_p}\right)/L$ where L_p is the hole diffusion length which is related to the lifetime and L is the horizontal distance from the middle-point of the window area to the middle P+ collector, as shown in Figure 3-2 (a). Calculation shows that the drift current density is about three orders of magnitude larger than the diffusion, therefore, the diffusion current density component is negligible and hole concentration is mainly determined by drift.

In the scenario of Figure 3-1, $\boldsymbol{J}_p\,(\boldsymbol{B})$ has x and y components while $\boldsymbol{J}_p\,(0)$ has only a component along x and $\boldsymbol{B}$ exists along z, B_z. Thus,

$$J_p\,(0) = q\mu_P\delta_P E_x + \frac{qD_p\delta_P}{L}\left(1 - e^{-L/L_p}\right) \cong q\mu_P\delta_P E_x\,, \tag{3.9}$$

$$J_{px}\,(B) = J_p\,(0) - \mu_P J_{py}\,(B)B_z, \tag{3.10}$$

$$J_{py}\,(B) = \mu_P J_{px}\,(B)B_z = \sigma_p E_y = q\mu_P\delta_P E_y, \tag{3.11}$$

$$tan\theta = \frac{J_{py}\,(B)}{J_{px}\,(B)} = \mu_p B \tag{3.12}$$

where, E_y is the Hall electric field, θ is the Hall angle. Since there is no electron current density in y direction at equilibrium,

$$J_{ny}\,(B) = q\mu_n\left(E_y - \mu_n B_z E_x\right) = 0, \tag{3.13}$$

and combining Equations (3.9) to (3.11), the excess hole concentration δ_P is obtained

$$\delta_P = J_{py}\,(B)/\left(q\mu_p^2 BE - \left(\mu_p B\right)^3 q\mu_n E\right) \tag{3.14}$$

where $J_{py}\,(B)$ can be deduced by measuring the current, I_m, of the middle collector .

Figure 3-2 shows the simulated holes' concentration profile and holes' current density in a pixel of WAS under electric field and a magnetic field varying from 0T to 3T. The magnetic field is pointing inward in a direction perpendicular to the paper. As shown in Figure 3-2, the middle P+

collector collects holes coming from a certain depth in the window area. At B=0T in (a), the current density presented by black lines is parallel to the surface in the window area and then slightly bends when reaching the collectors' region. While increasing the magnetic field, holes move up under the Lorenz force, and the Hall angle increases, allowing the collection of holes generated deeper in the N-well, as shown by the current density lines in (b), (c) and (d) for 1, 2 and 3 T respectively. Hence, by sweeping the magnetic field, it is possible to measure the excess holes' concentration along the depth.

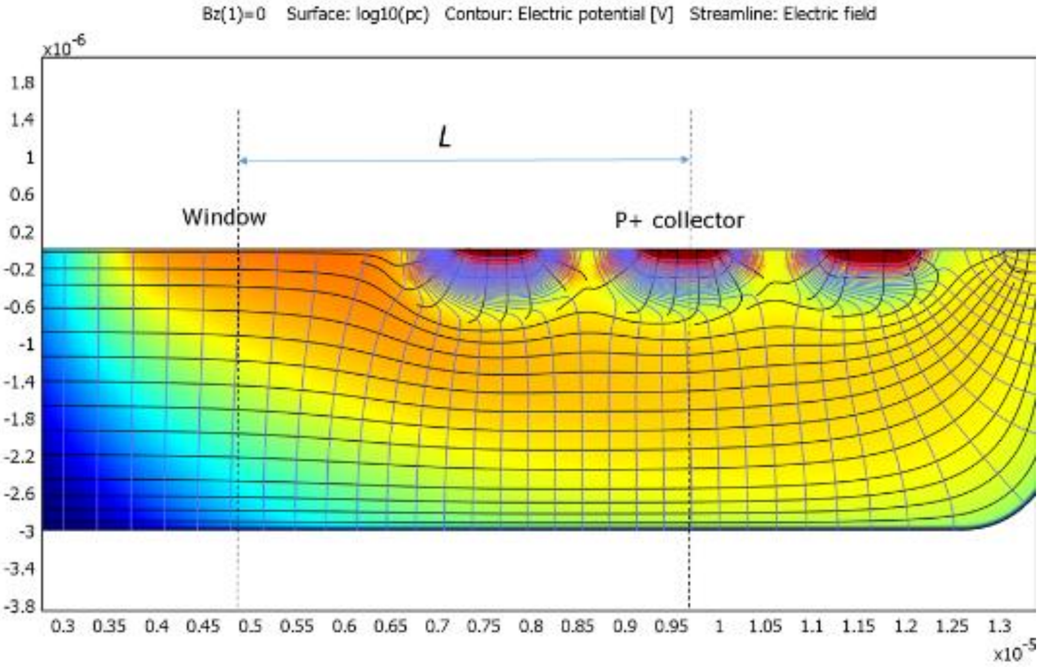

Figure 3-2 (a)

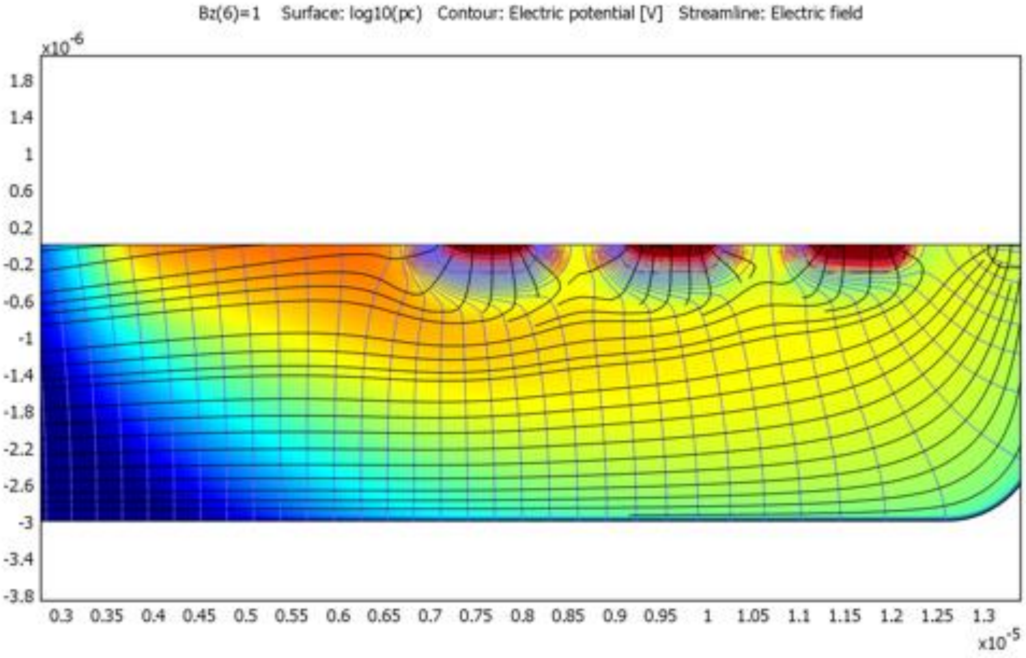

Figure 3-2 (b)

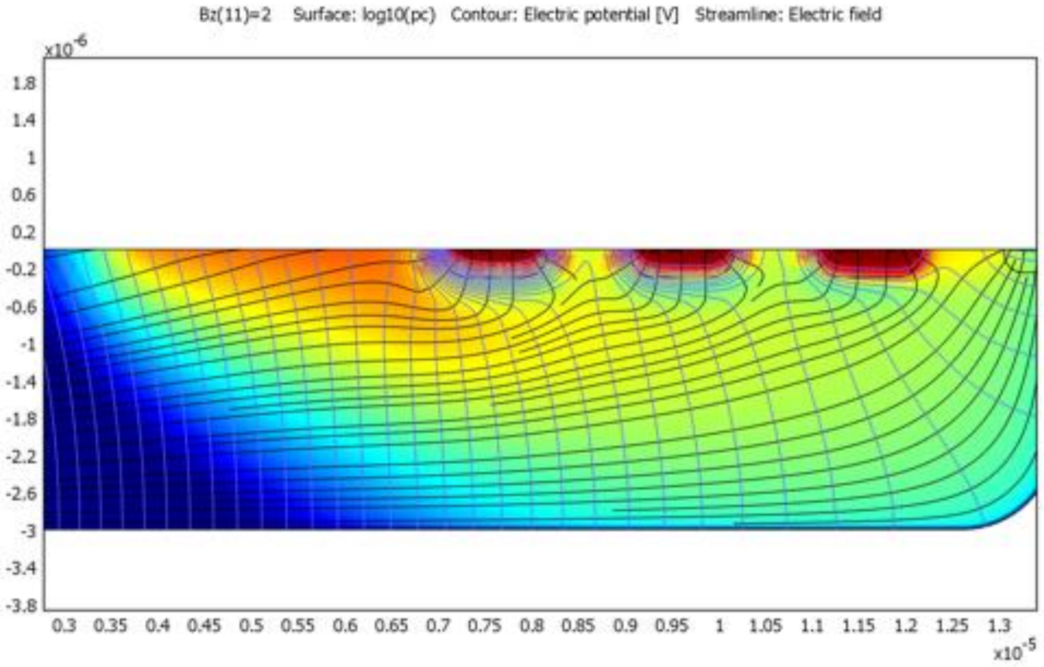

Figure 3-2 (c)

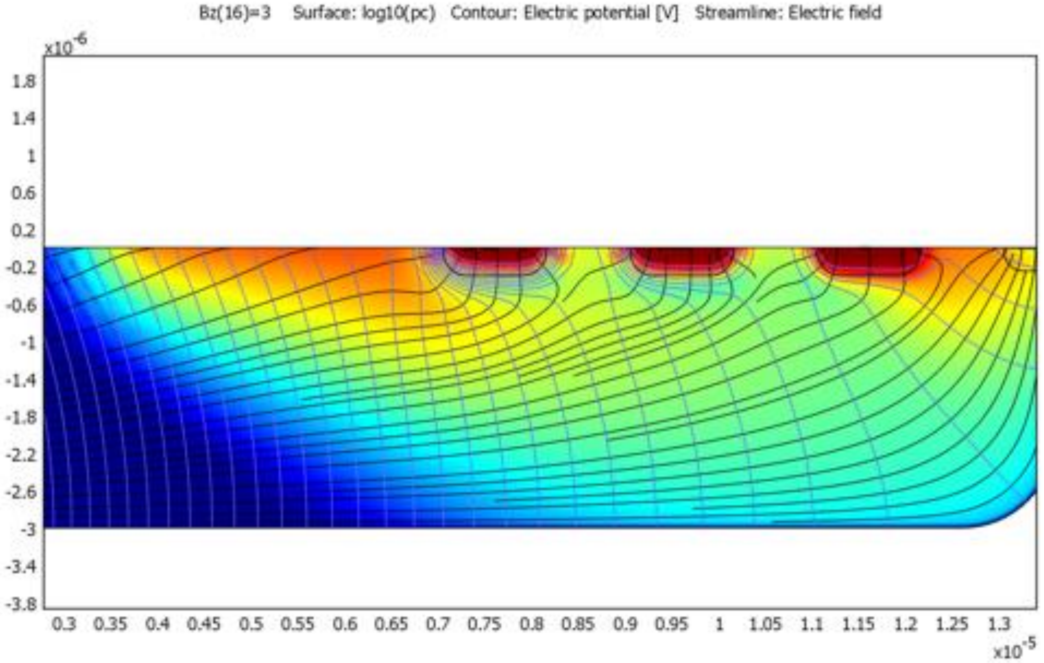

Figure 3-2 (d)

Figure 3-2 COMSOL^{TM} modeled results of a pixel at magnetic flux density, B= (a) 0T, (b) 1T, (c) 2T, and (d) 3T. The red area represents the high concentration region, and the low concentration region is in blue. The black lines illustrate the electric field orientation, and the blue lines represent the electric potential.

3.3.3 Experiment details and data analysis

In this section, important experiment details including the pixel array architecture of the WAS are presented, and experimental results validate the behavior of the proposed sensor.

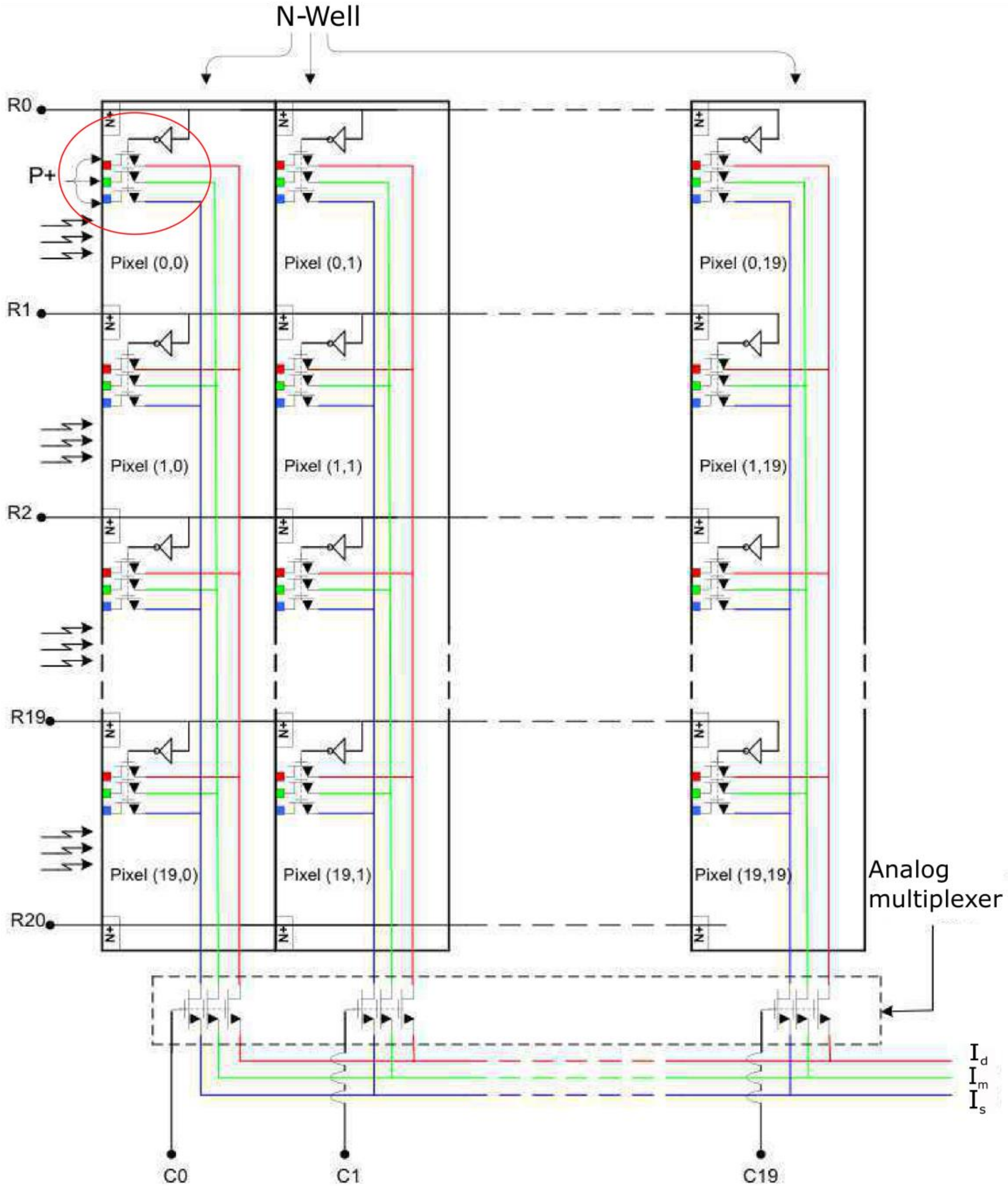

Figure 3-3 Architecture of the pixel array of the WAS prototype.

As illustrated in Figure 3-3, the WAS is composed of an array of 20x20 pixels along with pass transistors in order to direct the collected currents row-wise and column-wise down to three common outputs to each I_s, I_m and I_d pixel collector. Benefits of disposing of the proposed spectrometer in an array include the increase of the dynamic range and the capability of using the array as a micro spectral imaging sensor.

Each pixel is composed of three NMOS transistors, as shown in the red circle. They link the collectors to the vertical buses, *t* when the row selector signals, *R0* to *R19*, are applied to their gates. The logic inverter allows the use of the same signal to establish an electric field in the pixel, and activate the row selection transistors. When *R0* is set to 0V and other rows are 5V, an electric field is generated in the pixels of the first row, oriented towards the N+ contact of the row *R0*. The NMOS transistors on the row are turned *ON* through a logic inverter, such as only pixels in the row '0' are activated. In addition, column selector transistors are selected by the column control signal to connect one pixel at a time to the output bus. To allow the measurement of small currents and reduce the noise bandwidth, each line of the output bus is connected to an off-chip integrating transimpedance amplifier, as shown in Figure 3-4.

Figure 3-5 shows the printed circuit board, on which the pixel array is bounded. The pixel array is fabricated in 0.5 μm CMOS technology. It is placed at the center between two electromagnetic poles, as shown in Figure 3-6. The control board contains all the components of the reading circuit. It is connected to the sensor board by a flexible flat cable. To eliminate the mechanical forces acting on the pixel array and thus to avoid disturbing the optical alignment, all the conductors are made of copper only, which is a diamagnetic material.

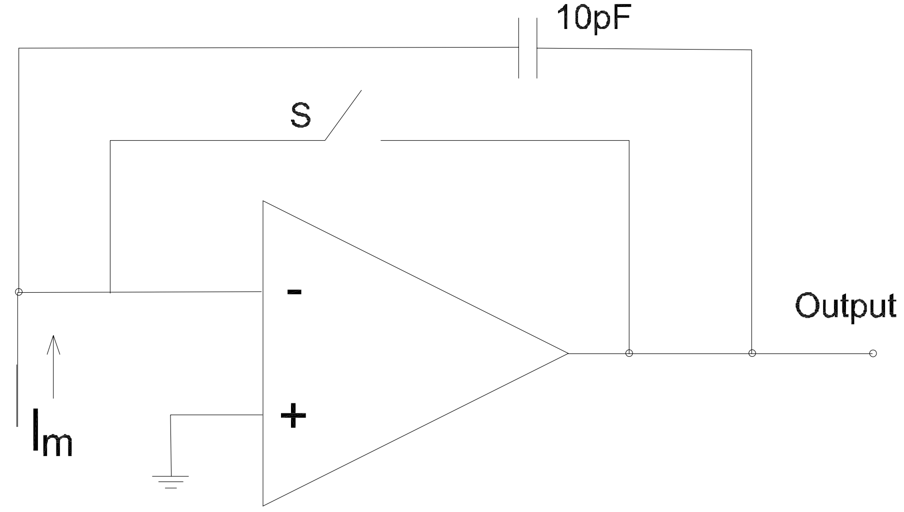

Figure 3-4 Schematic figure of an integrating transimpedance amplifier. The switch S is used to reset the capacitor after a pre-determine integration time.

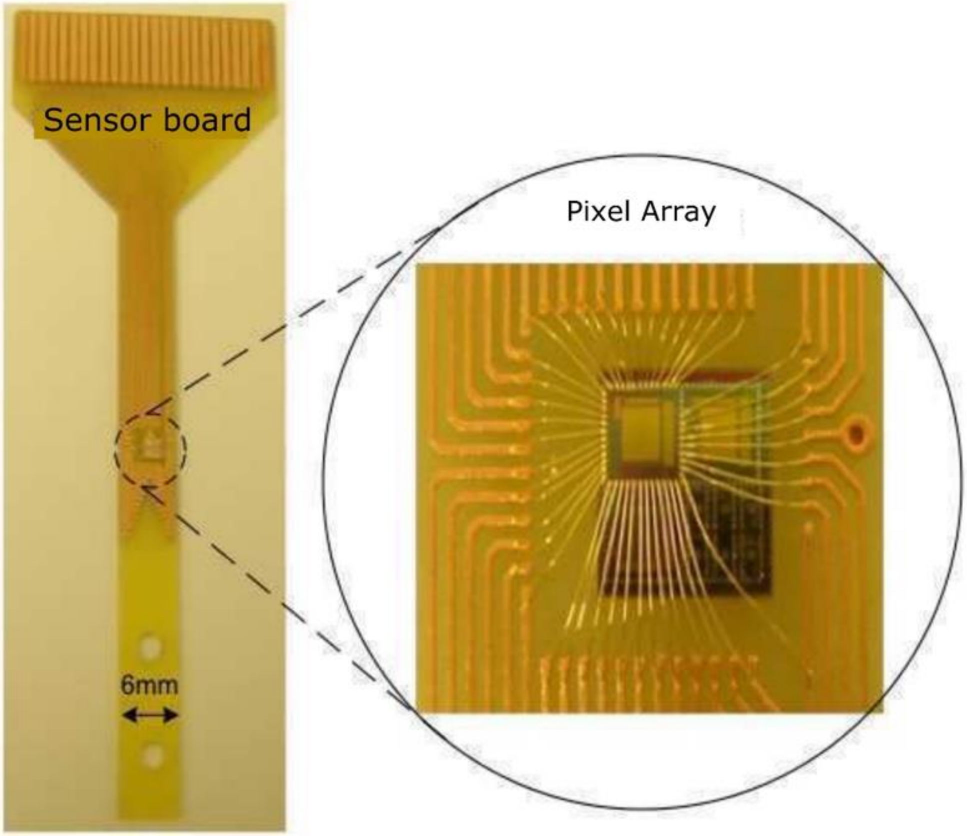

Figure 3-5 The sensor board hosting the pixel array chip.

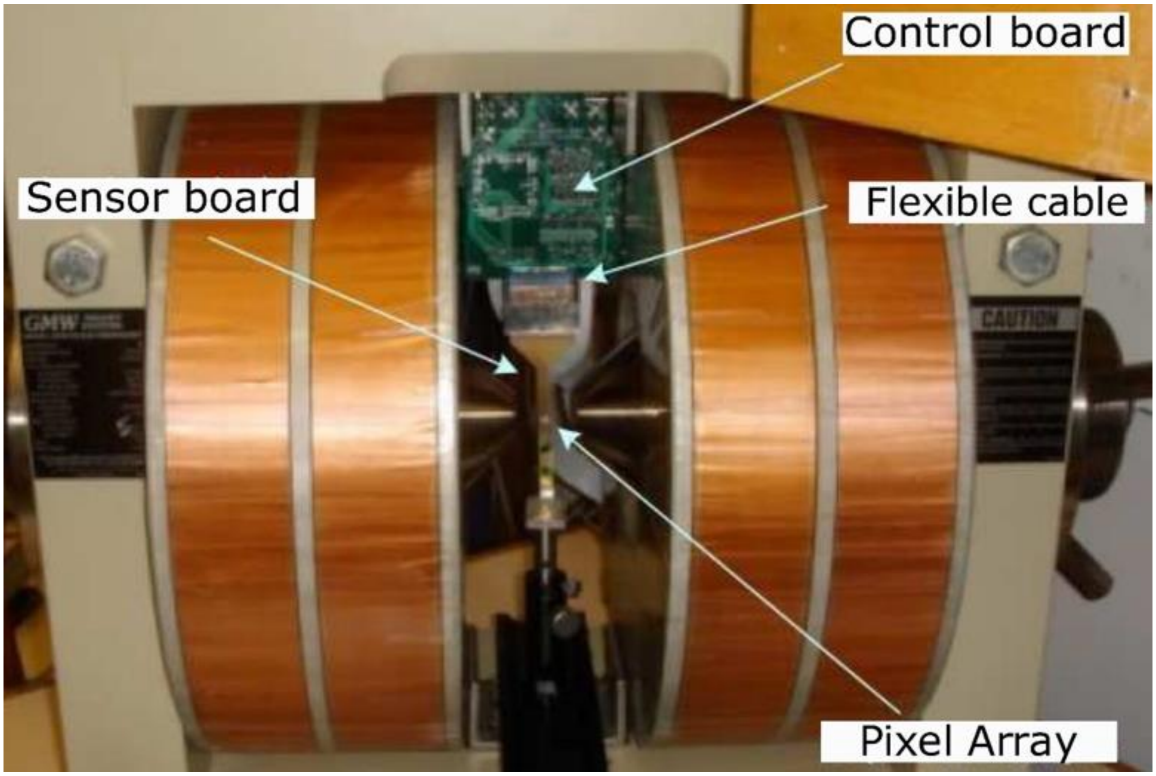

Figure 3-6 Experimental setup uses to test the WAS prototype.

The spectrometer is placed in an adjustable electromagnetic field and is illuminated by a light source at different irradiances and wavelength. The intensity of the magnetic field between the two poles depends strongly on the distance between them and the diameter of their external faces. The objective is, therefore, to have the part of the sensor board hosting the chip as slim as possible in order to obtain a wide range of magnetic field values between the two poles.

Figure 3-7 gives the experimental relationship of the reciprocal of detected excess holes' concentration versus depth. The concentration δ_P is derived from $J_{py}(B) = VC/tA$ and Equation 3-14,

$$\delta_P = VC/[tA\left(q\mu_p^2BE + \frac{qD_p}{L}\left(1 - e^{-L/L_p}\right)\mu_pB - \left(\mu_pB\right)^3 q\mu_nE\right)] \tag{3.15}$$

where C is the capacitor (10pF) of the integrating transimpedance amplifier as seen in Figure 3-4, t is the integration time, A is the surface area of a P+ collector, and V is the amplifier output voltage difference obtained with and without illumination. The subtraction is performed during data processing in order to remove the effect of the dark current on the P+ collector. The depth value $|y|$ as introduced in Equation 1 is derived based on the Hall Angle θ which is function of the magnetic field B_z,

$$|y| = L\, tan\theta \tag{3.16}$$

Figure 3-7, chromatic illumination results at 470 nm, 530 nm, and 640 nm, are represented in blue, green and red, respectively. The chromatic illuminations have been obtained from a halogen lamp with 70 nm bandwidth color filters. Excess holes' concentration is calculated according to Equation (3.15) from the measured voltages under three incident illumination irradiances (200μW/cm^2, 400μW/cm^2, and 800μW/cm^2). As seen on the graph, as the irradiance increases, the $1/\delta_P$vs $|y|$ relationships becomes more linear with slope values converging toward a constant as predicted by Equation (3.7) at high excess holes' concentrations where the Auger recombination mechanism is dominant. For each irradiance, the concentration generated by the 470 nm wavelength photons exhibits higher values due to the fact that penetration depth decreases for high energy (shorter wavelength) photons. That trend is also confirmed by concentrations produced by green photons (530 nm) being larger than the one of the red photons (640 nm).

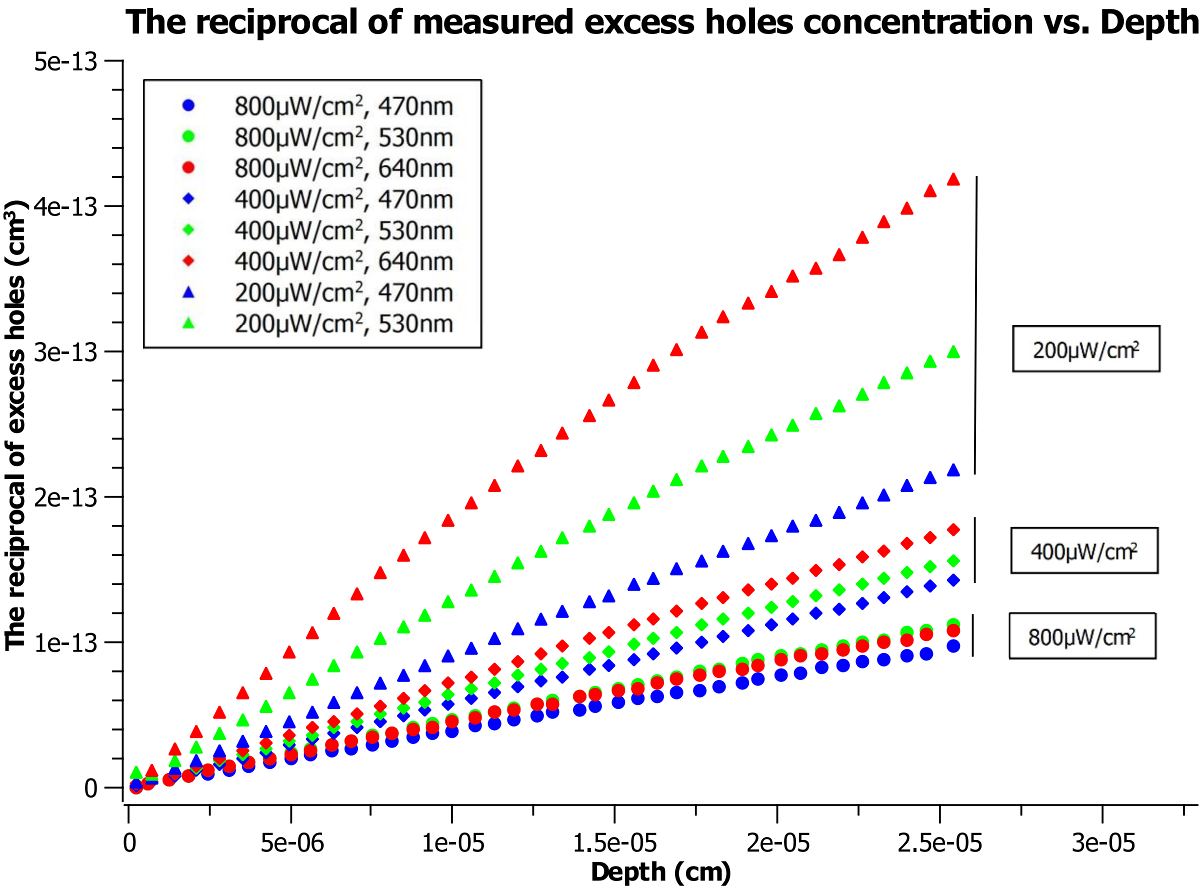

Figure 3-7 The reciprocal of detected excess holes concentration variation obtained by sweeping the magnetic field for several illumination irradiances.

3.4 Application as a spectrometer

In order to use the WAS as a spectrometer, the substrate must be in the SRH recombination regime where it is independent of the excess carrier concentration. We assume that photo-generated holes coming from different wavelength are additive, hence a linear system of equation can relate the irradiance of the light signal spread over a given spectrum to the collector currents. Through a calibration procedure, a system of linear equation can be built. Figure 3-8 illustrates the experimental curves of current density of the middle P+ collector as a function of the irradiance for three wavelengths, λ=470 nm , 590 nm and 660 nm, for two constant magnetic fields, 2.8 T and 1.0 T. The graph depicts quasi-linear relationships of current densities as a function of irradiances.

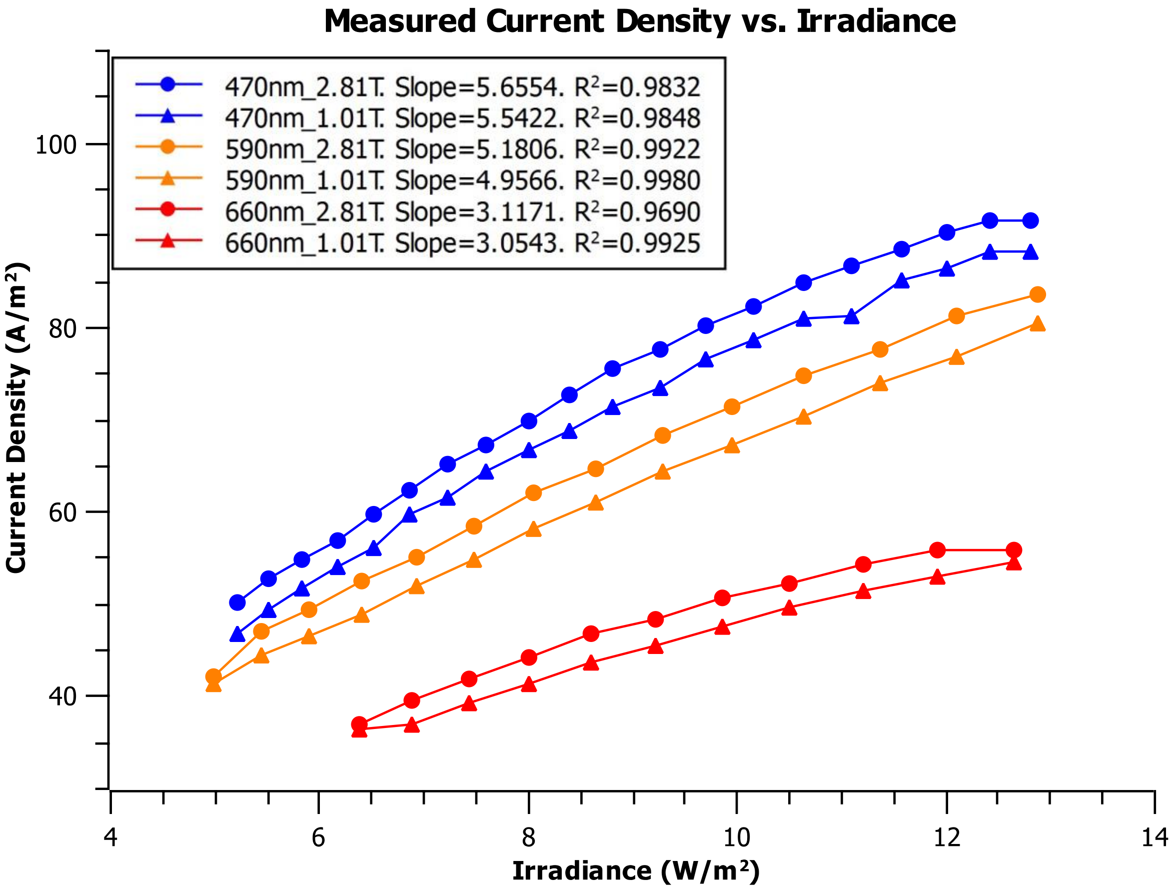

Figure 3-8 Measured current density as a quasi-linear function of the irradiance of 470 nm (blue), 590 nm (orange) and 660 nm (red), at B=2.81T (round) and 1.01T (triangle).

For an illumination composed of *n* discrete wavelengths, the current density *J*, can be expressed as

$$J = m_{\lambda 1} I_{\lambda 1} + m_{\lambda 2} I_{\lambda 2} + \cdots m_{\lambda n} I_{\lambda n} + n J_0 \tag{3.17}$$

where terms $I_{\lambda x}$ are the irradiance of the wavelength, λ_x, $m_{\lambda x}$ are the slopes of the current density versus irradiance relationship for λ_x and J_0 is the current density collected in the dark. Equation (3.17) represents a linear equation with *n* unknown $I_{\lambda x}$. Terms, $m_{\lambda x}$ have been measured previously from *n* chromatic filters having non-overlapping band pass and a center wavelength, λ_x. In order to solve Equation (3.17), we need a set of *n* equations. Given that the slopes of the *J* vs $I_{\lambda x}$ relationships vary not only with respect to the wavelength but also with respect to the magnetic field, it is then possible to obtain the following solvable system of equations,

$$J_{B1} = m_{B1,\lambda 1}I_{\lambda 1} + m_{B1,\lambda 2}I_{\lambda 2} + \cdots m_{B1,\lambda n}I_{\lambda n} + nJ_{B1,0}$$

$$J_{B2} = m_{B2,\lambda 1}I_{\lambda 1} + m_{B2,\lambda 2}I_{\lambda 2} + \cdots m_{B2,\lambda n}I_{\lambda n} + nJ_{B2,0} \tag{3.18}$$

$$\cdots$$

$$J_{Bn} = m_{Bn,\lambda 1}I_{\lambda 1} + m_{Bn,\lambda 2}I_{\lambda 2} + \cdots m_{Bn,\lambda n}I_{\lambda n} + nJ_{Bn,0}$$

where the suffix Bx indicates different magnetic field values. Hence, Equation (3.18) can be written in a matrix form,

$$J_B = M_{B\lambda}I_\lambda + J_{B,0} \tag{3.19}$$

where J_B and $J_{B,0}$ are the $n\times 1$ vector representing the measured current densities with and without illumination respectively, $M_{B\lambda}$ is the $n\times n$ matrix of the J_{Bx} vs $I_{\lambda x}$ slopes and I_λ is the $n\times 1$ vector of the irradiances. Therefore, the solution can be found from

$$I_\lambda = (J_B - J_{B,0})M_{B\lambda}^{-1}. \tag{3.20}$$

Coefficients of matrix $M_{B\lambda}$ are obtained from the slopes of calibration curves as the ones shown in Figure 3-8.

3.5 Conclusion

A novel spectrum detection method is proposed, and the mechanism is discussed in this article. The detection principle is based on the wavelength absorption in silicon where the photon-generated excess holes' concentration is a function of depth, wavelength, and irradiance. Variable magnetic field enables the measurement of the excess carrier concentration profile as a function of depth. Experimental results of collected current densities as a function of irradiances for different magnetic fields have validated the detection principle that relies on the additive property of photo-generated carriers when the device is in the SRH recombination regime. Those quasi-linear relationships are employed to determine the coefficients of a matrix used to solve algebraically a set of linear equations linking the measured current densities to the wavelength spectrum of the incident light. The small footprint of the WAS and its compatibility with standard CMOS fabrication processes allow for the design of an array which enables applications in the field of spectral imaging. Future work will be focusing on improving the current density vs. magnetic field linearity on a wider dynamic range by modifying the pixel geometry and implementing the WAS in smaller feature size CMOS processes.

CHAPTER 4 RESOLUTION ANALYSIS

4.1 Definition of Resolution

The resolution is a crucial parameter for a spectrometer. It is necessary to calculate the resolution of the WAS to understand its ability, limitation, and the ways to improve it. No magnetic field is considered to simplify the analysis.

The spectrometer resolution is defined as:

$$\mathrm{R} = \frac{\lambda}{\Delta\lambda} \tag{4.1}$$

where $\Delta\lambda$ is called the resolving power, which is the minimal wavelength difference that can be distinguished.

4.2 The resolution of the WAS

The WAS doesn't detect the wavelength directly, instead, it detects the hole current. Thus, its resolving power is limited by the minimum detectable current. The $\Delta\delta$ is defined as the minimal detected carrier concentration variation, which is determined by the shot noise [50]:

$$i_n^2 = 2qI_{DC}\Delta f \tag{4.2}$$

$$\Delta\delta = \sqrt{i_n^2}/(q) \tag{4.3}$$

I_{DC} is the detected current, the experimental value is approximately 10^{-12}A. Δf, 10 MHz, is the bandwidth of the oscilloscope employed to measure the current for the prototype WAS. The black line in Figure 4-1 represents the $\Delta\delta$.

For the WAS prototype, without the magnetic field, the difference in excess holes' concentration of two wavelengths is expressed as:

$$\Delta\delta' = \left| \int_{\mathrm{y}_1}^{\mathrm{y}_2} \alpha_1 \mathrm{I}_1 \mathrm{e}^{-\alpha_1 \mathrm{y}} \mathrm{dy} - \int_{\mathrm{y}_1}^{\mathrm{y}_2} \alpha_2 \mathrm{I}_2 \mathrm{e}^{-\alpha_2 \mathrm{y}} \mathrm{dy} \right| \tag{4.4}$$

where y_1 and y_2 are the vertical boundaries of the region where the carriers are collected. As shown in Figure 4-1, $\Delta\delta'$ is calculated for various wavelengths, 450 nm (blue curve), 550 nm (green curve), 650 nm (cyan curve), and 750 nm (red curve), respectively.

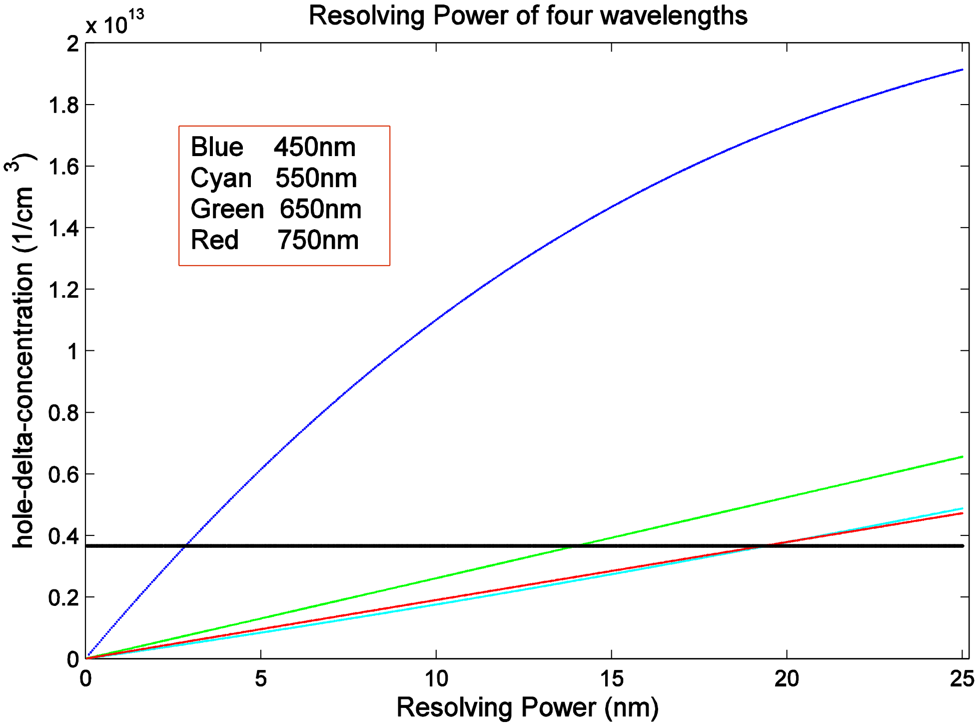

Figure 4-1 The calculated resolving power vs. wavelength by MATLAB, at the same incident power. The red curve and the cyan curve are almost coincident.

When $\Delta\delta = \Delta\delta'$, the abscissa of the intersection is the resolving power. In Figure 4-1, the resolving power is within a range of 3 nm to 19 nm over the range (450 nm to 750 nm).

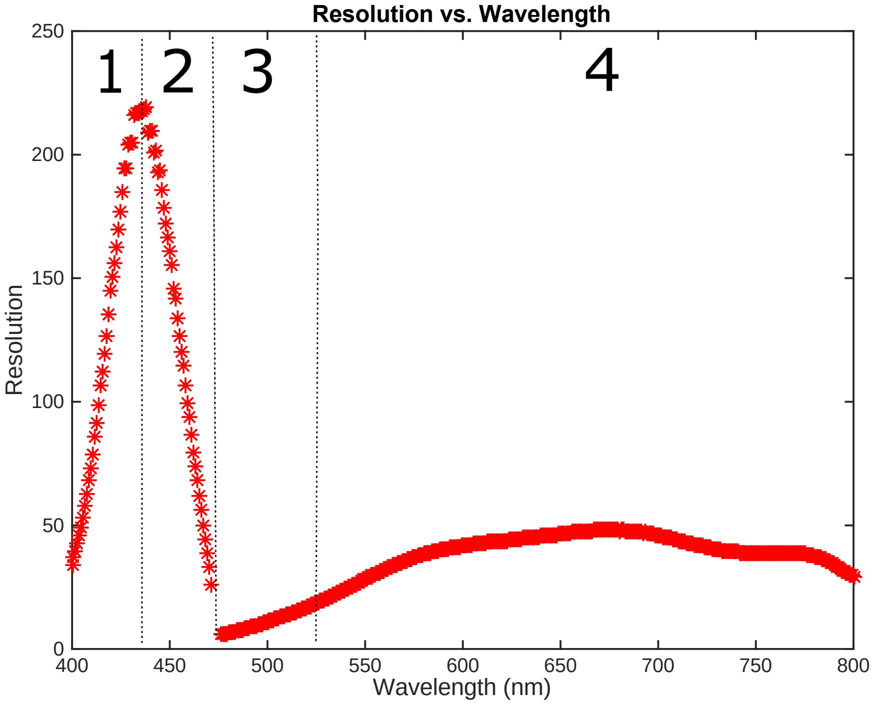

Figure 4-2 The calculated resolution vs wavelength at the same incident power.

Figure 4-2 gives the resolution of the WAS over the range 400 nm to 800 nm. The best resolution reaches 219 at the 438 nm, and the smallest resolution is around 10 at 475 nm. The non-linear resolution-wavelength relationship indicates that the resolution of the WAS is determined by mainly two factors: the absorption coefficient and geometry. The 400 nm to 800 nm range is divided into four zones, and the resolution in each zone will be discussed, respectively. Zone 1: 400 nm to 438 nm; Zone 2: 438 nm to 475 nm; Zone 3: 475 nm to 525 nm; Zone 4: 525 nm to 800 nm. As shown in Figure 4-2.

Zone 1 & 2: From Figure 2-2, it is clear that, wavelengths in Zone 1 and Zone 2 have much higher absorption coefficient and therefore generates carriers closer to the surface which form a larger current I_m. In addition, this range has a big slope ${d\alpha}/_{d\lambda}$, which induces a bigger difference of carrier concentration generated by the adjacent wavelengths and explains the higher resolution.

Zone 1: For the reasons stated above, should have higher resolution than Zone 2. However, the resolution drops with the wavelength becoming shorter. This is the same effect as observed in Figure 4-3 where carriers closer to the surface are collected by the left P+ electrode and have less contribution to the current I_m.

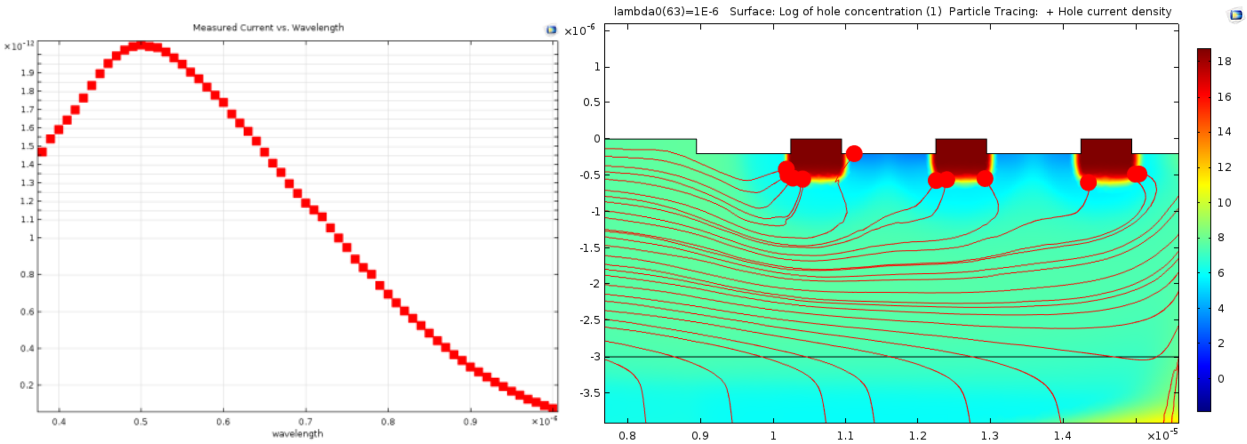

Figure 4-3 The three P+ electrodes collect holes coming from different depths.

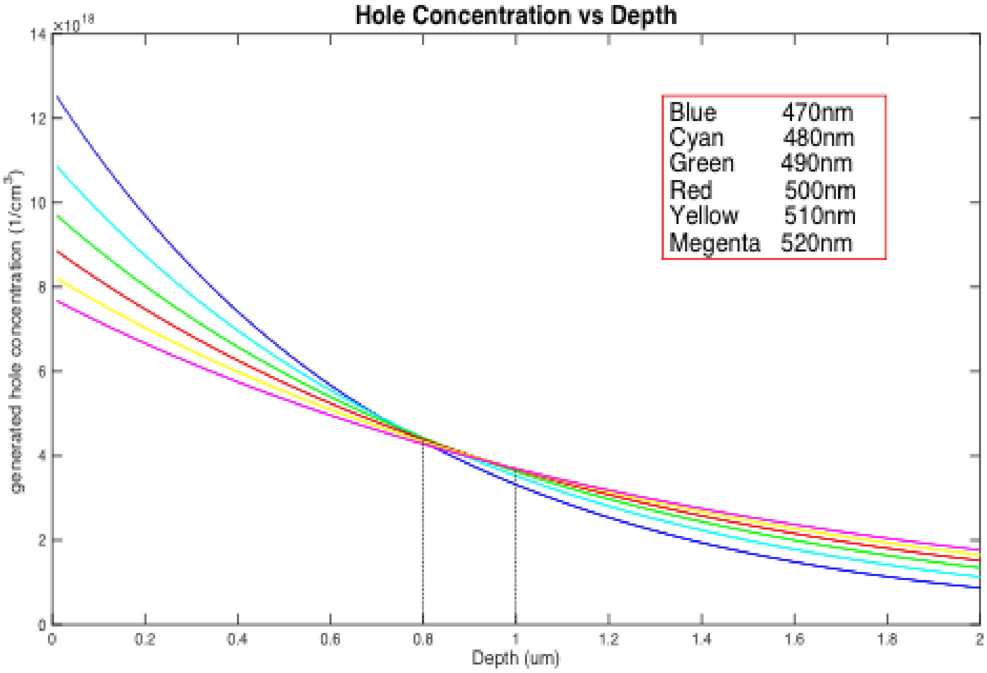

Figure 4-4 Photo-Generated hole carrier concentration along the depth. The dash lines show the boundaries of the holes concentration integration.

Zone 4: As seen in Figure 2-2, the 475 nm is an inflection point, after which the $^{d\alpha}/_{d\lambda}$ becomes smaller. This will decrease the resolution, as shown in Figure 4-2. In this region, the resolution is in the vicinity of 30 for a maximum of 50.

Zone 3: This is a special range because the absorption coefficient is still high but the resolution is very low. The Equation 4-4 indicates that the low resolution is determined by the small difference of the generated carrier concentration. Actually, the concentration is an integration result between 0.8 μm and 1 μm, not from a single depth, as shown in the Figure 4-4. The integration range is limited by the designed geometry, as shown in Figure 4-3. A different geometry will bring a different integration range. Figure 4-4 gives the concentration variation with the depth for several wavelengths (from 475 nm to 525 nm). It is clear that the integration results of these wavelengths are similar due to actual position of the depth integration limits (from 0.8 μm to 1 μm). It explains why the WAS prototype has smallest resolution in Zone 3.

For the current WAS prototype, the best theoretical resolution occurs in Zones 1 and 2. The Zone 4 has a stable resolution, and Zone 3 should be avoided for high accuracy application.

To expand the best detection spectrum region, the geometry and structure modification is necessary. The possible improvements may include: a smaller depth for the left P+ electrode, more P+ electrodes, and a larger distance between the electrodes.

4.3 Conclusion

The study on resolution of the Wavelength Absorption Spectrometer (WAS) based on experimental data and a finite element model proved its functionality. The theoretical calculation predicts that the resolution of the WAS could reach around 219 depending on the collectors' junction shot noise. The structure requires further development for better performance.

CHAPTER 5 SOLUTION OF CONTINUITY EQUATION

In previous chapters, we analyzed the photo-generated excess carriers' generation, recombination and transportation under an electric and magnetic field. In this chapter, we pay attention to the effect of some parameters of the continuity equation in order to get a full view of the mechanisms of generation and recombination. All discussions are related to the one dimensional photo-generated excess holes without electrical and magnetic field.

The photo-generated excess holes' concentration is described by the continuity equation.

$$D_p \frac{d^2 \delta_p(|y|)}{dy^2} - \frac{\delta_p(|y|)}{\tau_p} + g_p = 0 \tag{5.1}$$

Where τ_p is the holes' lifetime, δ_p is the excess holes' concentration, D_p, the diffusion coefficient [48], and, $|y|$, the depth from the surface ($y=0$). For an illumination irradiance, P, at a specific wavelength, λ, the generation rate, g_p, is defined as [20]

$$g_p = \frac{P\lambda}{hc} \alpha_\lambda (1 - \mathrm{Re}) e^{-\alpha_\lambda |y|} \tag{5.2}$$

where α_λ is the absorption coefficient and Re is the reflectivity at the Si/SiO_2 interface.

5.1 Boundary conditions

Different boundary conditions result in different solutions to Equation (5.1). For the WAS prototype, there are four possible boundary conditions. All of them are discussed in this chapter.

Photons generate excess carriers in N-well and P-substrate regions. However, only the N-well region is of interest since the collected holes come mainly from the N-well. The reversed-biased PN junction prevents the abundant holes in the P-substrate to be collected.

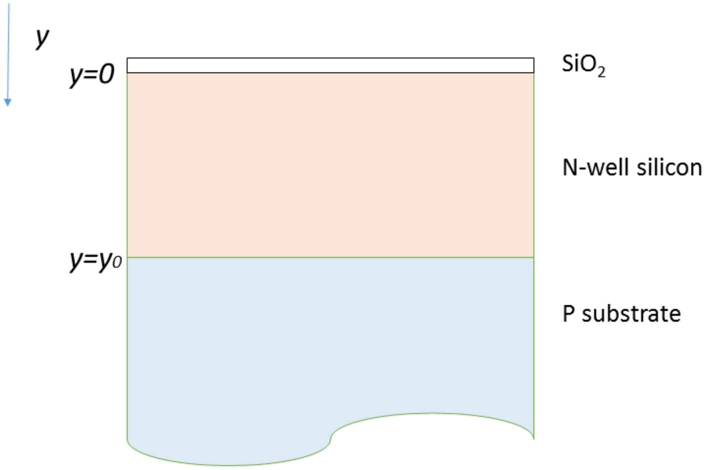

Figure 5-1 Schematic figure of N-well region with boundaries.

As shown in Figure 5-1, N-well region has two boundaries: interface with SiO_2 and interface with P-substrate. The interface between N-well and SiO_2 has two possible boundary conditions: $\delta_p'(0) = \frac{S}{D_p}\delta_p(0)$ and $\delta_p(0) = g_p(0)$. S is the surface recombination velocity. For a typical Si/SiO_2 interface, the value of S varies from 1 to 100 cm/s [51], and will be discussed later. The condition $\delta_p(0) = g_p(0)$ is an ideal situation that is used in Equation 3-7 to derive the analytical solution to the continuity equation under the assumption of high excess carriers' concentration. The condition $\delta_p'(0) = \frac{S}{D_p}\delta_p(0)$ is more accurate and is employed in this chapter. At the junction between the N-well and the P-substrate, $\delta_p(y_0) = 0$, where y_0 is the depth of the junction. Another boundary condition is $\delta_p(\infty) = 0$ that means no carrier is generated at the infinite depth.

Therefore, we have two boundary condition cases to Equation (5.1).

Case 1.

$$\delta_p'(0) = \frac{S}{D_p}\delta_p(0),\ \delta_p(y_0) = 0 \tag{5.3}$$

Case 2.

$$\delta_p'(0) = \frac{S}{D_p} g_p(0), \quad \delta_p(\infty) = 0 \tag{5.4}$$

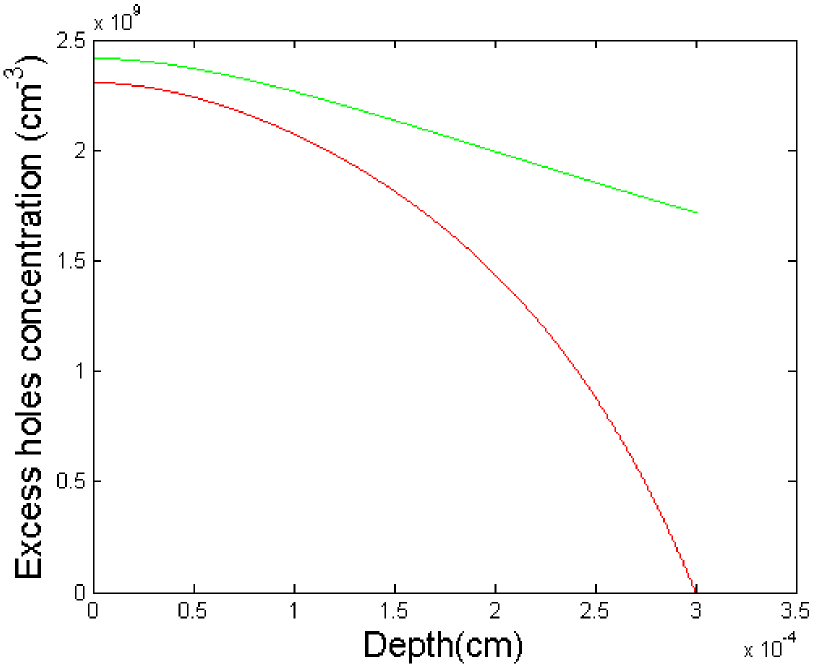

Figure 5-2 Excess holes' concentration vs depth for two boundary condition cases.

Figure 5-2 gives the excess holes' concentration variation along penetrated depth for two cases of boundary conditions. Red and green curves represent Case 1 and Case 2 respectively. Concentration in Case 1 drops faster than Case 2 due to its convergence to 0 in a smaller range.

This is a one-dimensional theoretical calculation along y-direction without an electric and a magnetic field. However, in the presence of an electric field, the condition $\delta_p(y_0) = 0$ is not valid anymore because there is holes' current along the PN junction.

5.2 Surface recombination velocity

Surface recombination velocity is a term to specify the recombination rate on a surface, usually varying between 1 to 100 cm/s for silicon [51]. Figure 5-3 demonstrates the effect of surface recombination velocity on excess carriers' concentration, where S=1 (blue), 10 (green), and 100 (red), respectively. Higher S will result in higher recombination and lower carriers' concentration as expected. The small difference observed on surface concentrations (*y*=0) illustrates that *S* doesn't have a significant influence on carrier concentration, therefore, we choose *S*=1 cm/s for all calculations in this thesis.

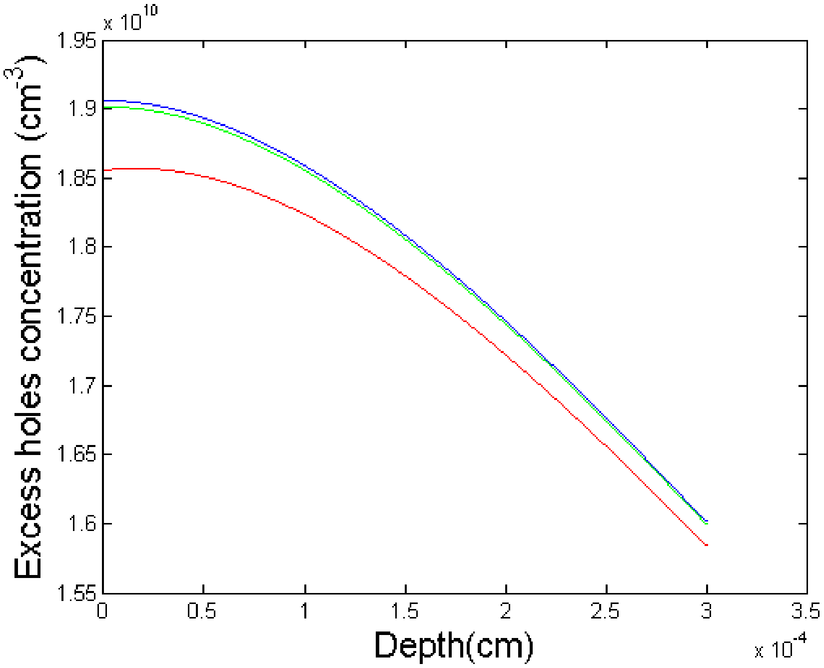

Figure 5-3 Carriers' concentration vs depth for several *S* values.

5.3 Carriers lifetime

The hole recombination lifetime, τ_P, is not constant and is determined by the Auger and the Shockley-Read-Hall (SRH) recombination mechanisms [20], [52], [53]

$$1/\tau_p = 1/\tau_{\text{Auger}} + 1/\tau_{\text{SRH}} \,, \tag{5.5}$$

where the Auger lifetime is [20]

$$\tau_{\text{Auger}} = 1/[\mathrm{C}_n(n_0^2 + 2n_0\delta_P + \delta_P^2) + \mathrm{C}_p(p_0^2 + 2p_0\delta_P + \delta_P^2)], \tag{5.6}$$

and the Shockley-Read-Hall lifetime is [20]

$$\tau_{\text{SRH}} = [\tau_{p-SRH}(n_0 + n_1 + \delta n) + \tau_{n-SRH}(p_0 + p_1 + \delta p)]/(p_0 + n_0 + \delta p) \tag{5.7}$$

where C_p and C_n are the Auger recombination coefficients for holes and electrons respectively, n_0 and p_0 are the equilibrium carrier densities, δn and δp are the excess carriers' densities, for electrons and holes respectively, n_1, p_1, τ_{p-SRH}, τ_{n-SRH} are defined as

$$n_1 = n_i \exp(\frac{E_T - E_i}{kT}) \, , p_1 = n_i \exp(-\frac{E_T - E_i}{kT}) \tag{5.8}$$

$$\tau_{p-SRH} = 1/\sigma_p v_{th} N_T \; , \; \tau_{n-SRH} = 1/\sigma_n v_{th} N_T \tag{5.9}$$

N_T is the impurity density, E_i is the intrinsic energy level, E_T is traps energy level in the band gap, capture cross sections for electrons and holes are σ_n and σ_p, respectively and v_{th} is the thermal velocity.

Low-level (*ll*) injection means that the excess minority carrier density is low compared to the equilibrium majority carrier density, $\Delta n \ll p_0$, and on the other hand, high-level (*hl*) injection means that $\Delta n \gg p_0$. For low level (*ll*),

$$\tau_{\mathrm{SRH}}(ll) \approx [\tau_{p-SRH} n_1 + \tau_{n-SRH} p_1]/p_0 \approx \tau_{n-SRH} \tag{5.10}$$

and for high-level (*hl*),

$$\tau_{\mathrm{SRH}}(hl) \approx \tau_{p-SRH} + \tau_{n-SRH} \tag{5.11}$$

The Auger lifetime is a function of holes' concentration (Equation (5.6)) and the SRH lifetime is determined by the impurity and defect densities (Equation (5.10) and (5.11)), which means the SRH lifetime is constant for one sensor.

From experimental data, holes' concentration in an equilibrium state in the WAS is around $10^{12} \sim 10^{16}$ cm^{-3}. This is considered as low concentration range and the SRH recombination mechanism is dominant. In this condition, it is reasonable to use a constant lifetime in theoretical calculations. A small range near the surface has a large concentration and the lifetime is mainly determined by Auger recombination. In the next section, we discuss on the effect of lifetime on the holes' concentration.

5.3.1 Constant Lifetime

When the SRH recombination mechanism is dominant, the carrier lifetime is constant. The minority carriers' lifetime in silicon varies from 0.1 ns to 100 ns depending on the doping concentration as reported [54]–[56]. Figure 5-4 shows the carrier concentration with five lifetimes: t = 1μs (a), 100ns (b), 10ns (c), 1ns (d), and 0.1 ns (e), respectively, with the boundary condition Equation (5.4). Shorter lifetime means higher recombination rate and reduces the holes' concentration. Lifetime has a significant effect on the value of concentration but slightly affects the shape of the curves.

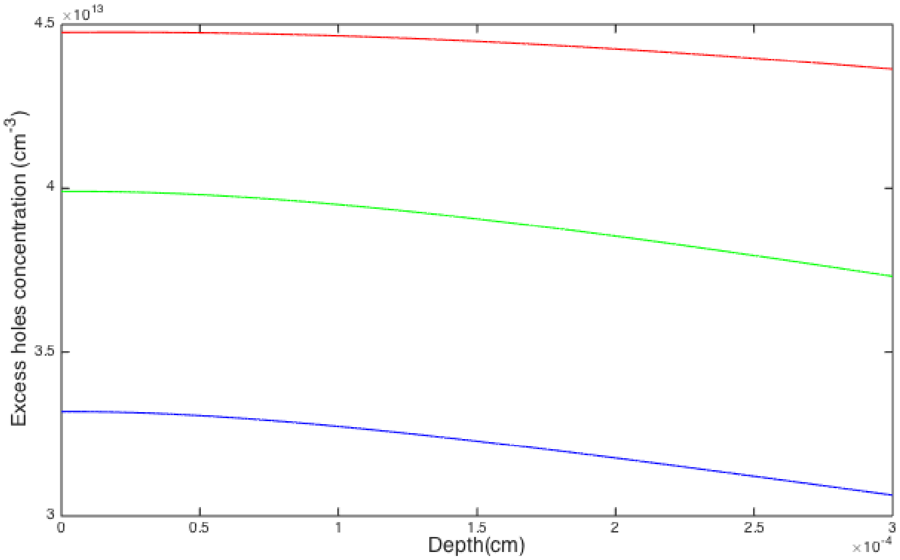

Figure 5-4 (a)

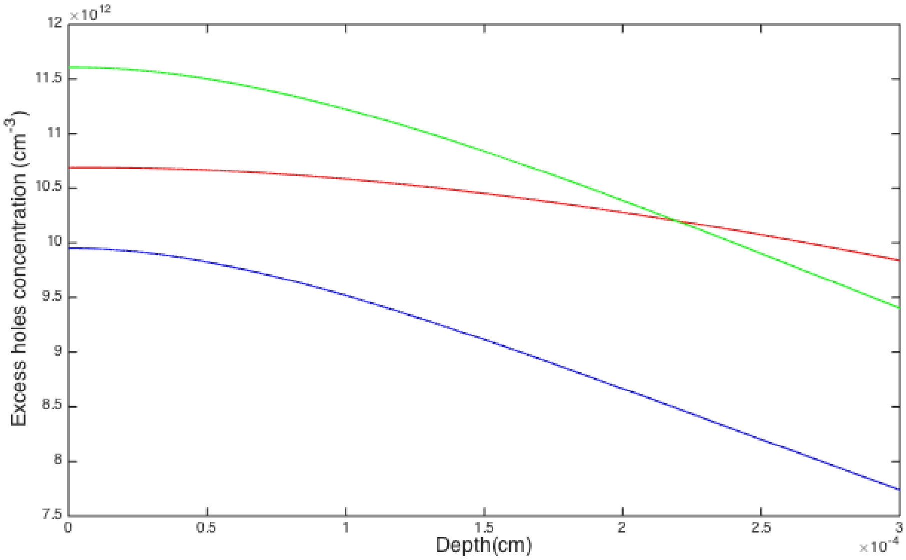

Figure 5-4 (b)

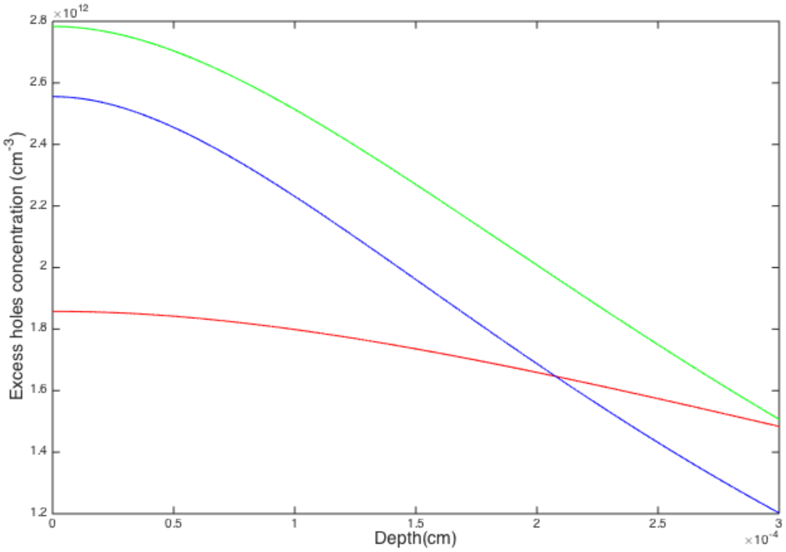

Figure 5-4 (c)

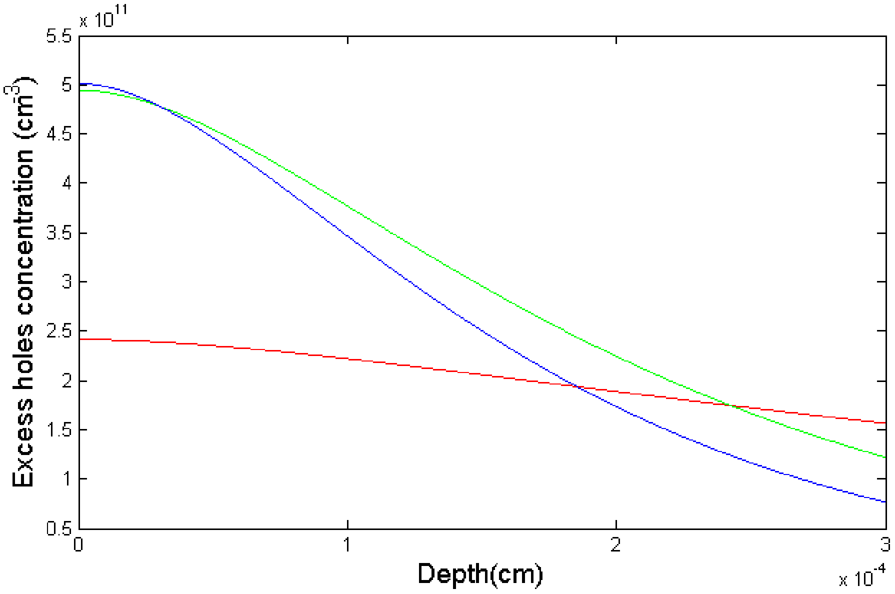

Figure 5-4 (d)

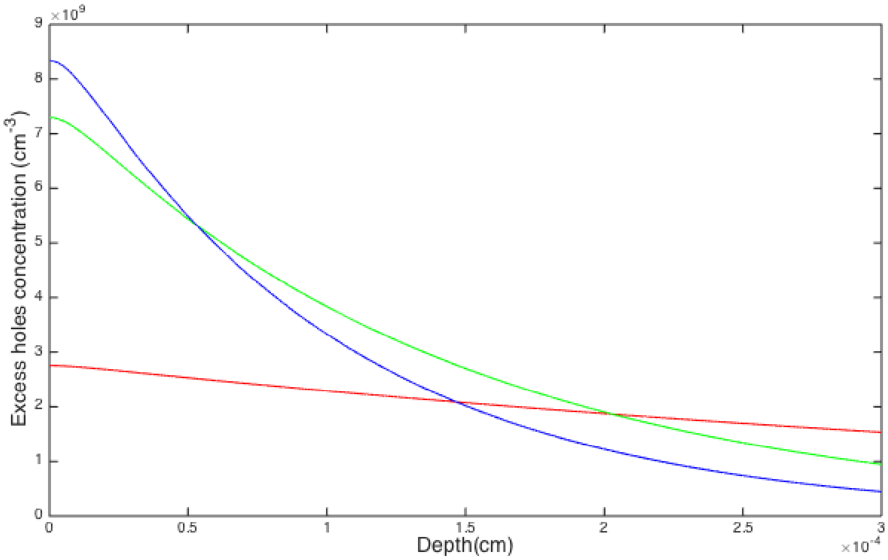

Figure 5-4 (e)

Figure 5-4 Carriers' concentration vs depth for several lifetimes,

t = 1μs (a), 100*n*s (b), 10*n*s (c), 1*n*s (d), and 0.1*n*s (e). Three wavelengths, 450*n*m (blue), 550*n*m (green), and 700*n*m (red), are employed with same incident power.

Compared Figure 5-4 with the modeled result in Figure 5-5, the hole lifetime in the WAS should be around 0.1 *n*s, or even shorter.

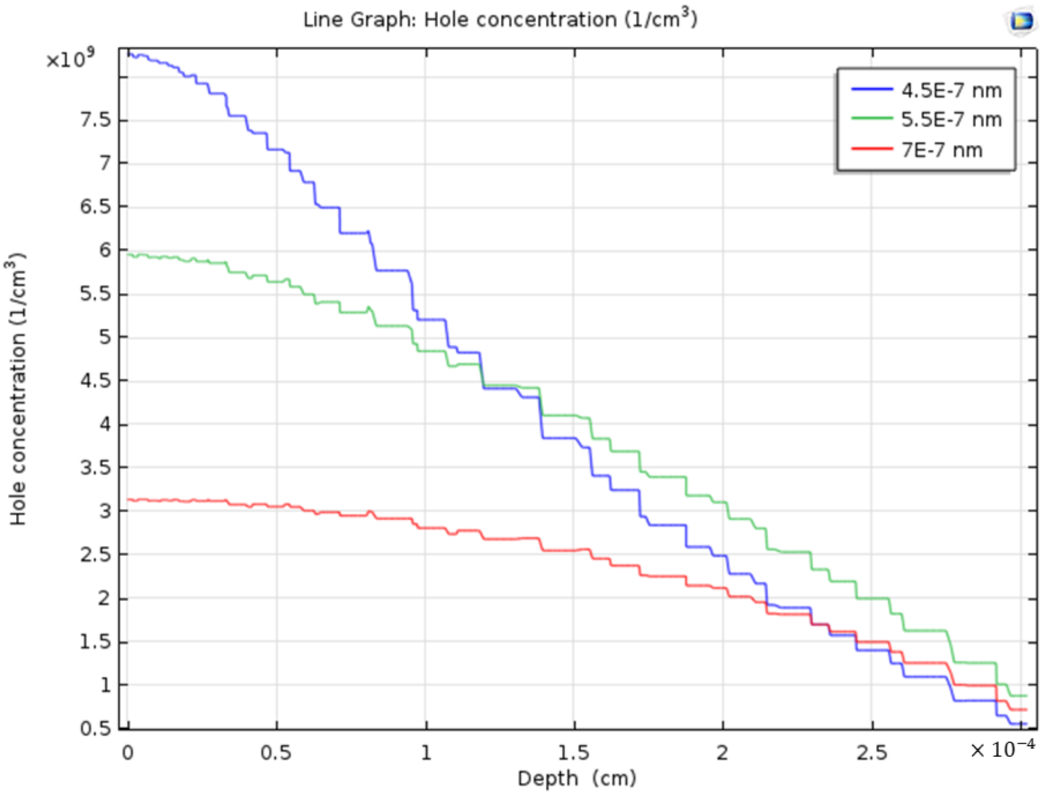

Figure 5-5 Concentration vs depth in the range of 0 μm to 3 μm, from COMSOL™, 450*n*m (blue), 550*n*m (green), and 700*n*m (red).

5.3.2 Variable Lifetime

Auger recombination lifetime is a function of holes' concentration, and also determines the concentration until an equilibrium state, thus we use iteration method to solve the Equation (5.1). When the concentration drops to a low level, the lifetime becomes SRH lifetime.

An estimated lifetime (1 *n*s) as an initial value is used to calculate the concentration, then use the concentration to derive a new lifetime, and repeat the process until it reaches convergence. Figure 5-6 gives the concentrations for three wavelengths, 450*n*m (blue), 550*n*m (green), and 700*n*m (red). The returned lifetime by iteration method is 1 μs for all wavelengths, which indicates the recombination mechanism is SRH recombination and this is verified by the holes' concentration, near 10^{12} cm^{-3}. However, since the lifetime reduces to SRH lifetime in all range, the high concentration area near the surface (small depth) is not calculated correctly. As a comparison,

Figure 5-5 gives the modeled concentration by COMSOL^{TM}. The iteration method gives larger lifetime and higher carrier concentration.

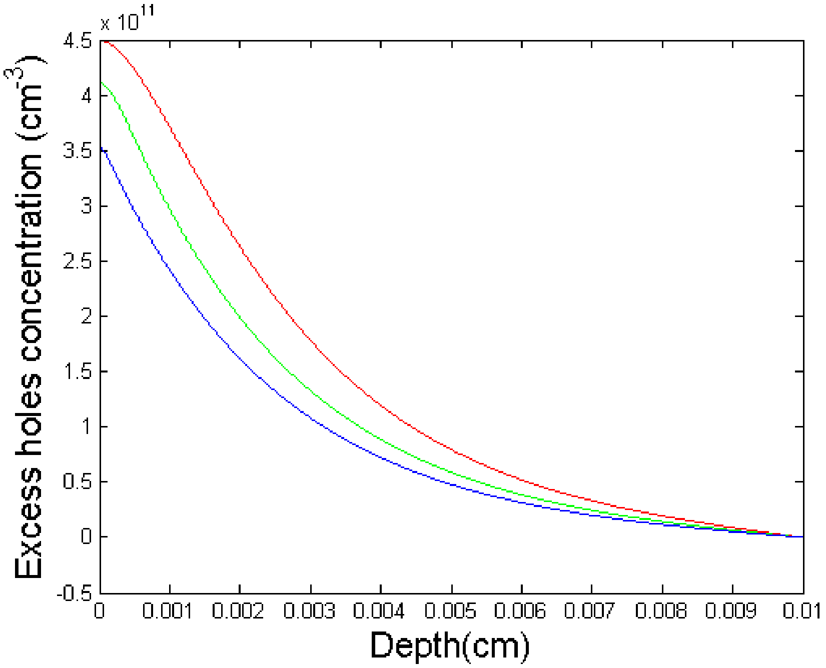

Figure 5-6 Carriers' concentration vs depth by iteration method for three wavelengths, 450*n*m (blue), 550*n*m (green), and 700*n*m (red).

5.4 Conclusion

In this chapter, we focus on the continuity equation and analyze the photo-generated excess carriers' concentration profile along the depth (one-dimension) at equilibrium state after generation-recombination process without the electric and magnetic field. Boundary conditions, surface recombination velocity and carriers' lifetime are discussed separately to explore their effect on the concentration profile. The surface recombination velocity doesn't have much effect while surface recombination velocity and carriers' lifetime impact more. Carriers' lifetime is a function of densities of impurities and carriers, and it will affect the carriers' concentration as well.

CHAPTER 6 FINITE ELEMENT METHOD MODELING

Finite element method (FEM), also known as Finite Element Analysis (FEA), is a numerical method to solve differential equations with boundary conditions in engineering and mathematical physics, usually employed in the fields of electromagnetics, mechanical structures, heat transfer, fluid flow,…etc. [1][2]. The method divides the problem into many smaller and simpler parts called finite elements, and transforms the differential equation into a system of algebraic equations.

COMSOL^{TM} is a multi-physics finite element method software [46]. The project WAS belonging to a multi-physics problem, thus in this thesis, all FEM models are simulated by COMSOL^{TM}, on two versions, v3.5a and v5.1. Version 5.1 has the *Semiconductor* module providing parameter settings including semiconductor materials, doping, diffusion, electric field, electrical contacts, generation, and recombination. Version 3.5a doesn't have the *Semiconductor* module, therefore, we use *Electrostatics* and *Convection and Diffusion* modules to simulate electric field and carriers' transportation, respectively. However, the v3.5a offers a better flexibility to define the electrical parameters in order to simulate Hall Effect in a 2D model, while the v5.1 doesn't.

6.1 Model Setup

In this part, a short demonstration is given to show the procedure to establish a COMSOL^{TM} model. A few key points which are not mentioned in the official guides will be emphasized. The v3.5a is an old version, and only few users are still working on it. Therefore, we use the v5.1 to introduce the procedure. The electrical parameter setting for Hall Effect will be explained on v3.5a.

For the WAS modeling, we start from a *Model Wizard*, choose *2D* for *Space Dimension* and *Semiconductor Module* for *Physics Interface*. Then we create a geometry of the WAS, as shown in Figure 6-1.

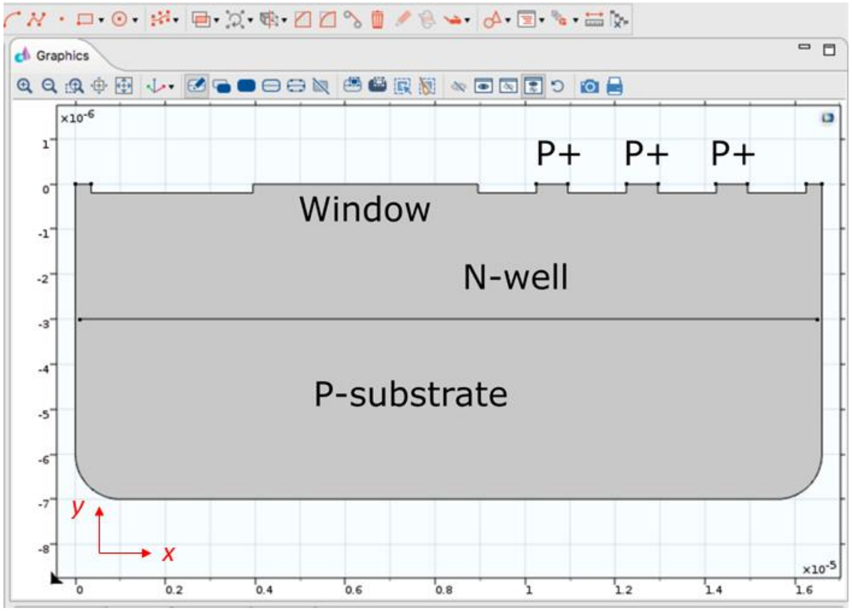

Figure 6-1 Geometry of the WAS model.

Figure 6-1 gives the complete geometry of the WAS. P-substrate, N-well region, Window area, three P+ collectors are marked. The notches on the top boundary model the effect of SiO_2, the insulation layer widely use in a CMOS fabrication process, hence the top boundary is set to 'Insulator'. Most corners are modified in arc in order to ease convergence. Convergence means that the error of the numerical solution matches the equation within a pre-defined relative error tolerance, usually less than 10^{-6}.

The next step is to define the parameters of the WAS, mainly including *Materials*, *Boundary conditions* (insulation, zero charge, continuity, contact), *Domains* (uniform doping, analytical doping, generation, SRH recombination, Auger recombination), and self-defined functions if necessary under *Definitions* tab, as shown in Figure 6-2.

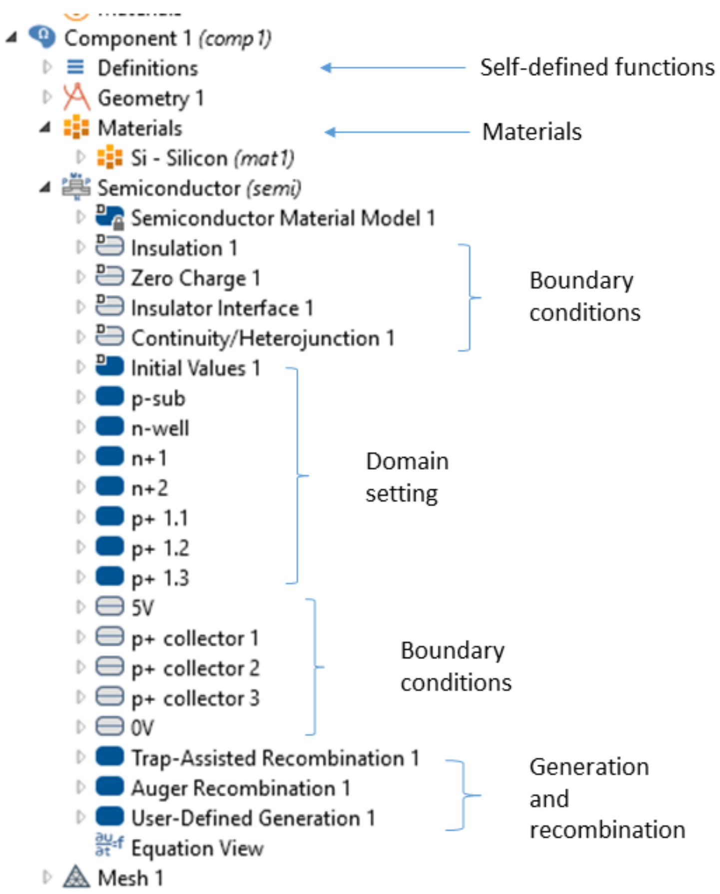

Self-defined functions

Materials

Boundary conditions

Domain setting

Boundary conditions

Generation and recombination

Figure 6-2 Semiconductor module setting.

Before solving the problem, a crucial step is to create a mesh, to break down the whole structure into infinite elements. The mesh size and shape have a significant effect on convergence. COMSOL^{TM} offers two mesh shapes, triangular and quadrilateral shape, and the former is commonly used. Large size may result in failure in convergence, while small size may take too much time to solve. A suggestion is to use the default mesh at first, then modify it for a better performance. Figure 6-3 illustrates the mesh for the WAS. A normal size is applied to all domains, and extremely fine size is used on all boundaries and interface between N-well and P-substrate. Small size in boundaries and discontinuity region helps to obtain convergence faster.

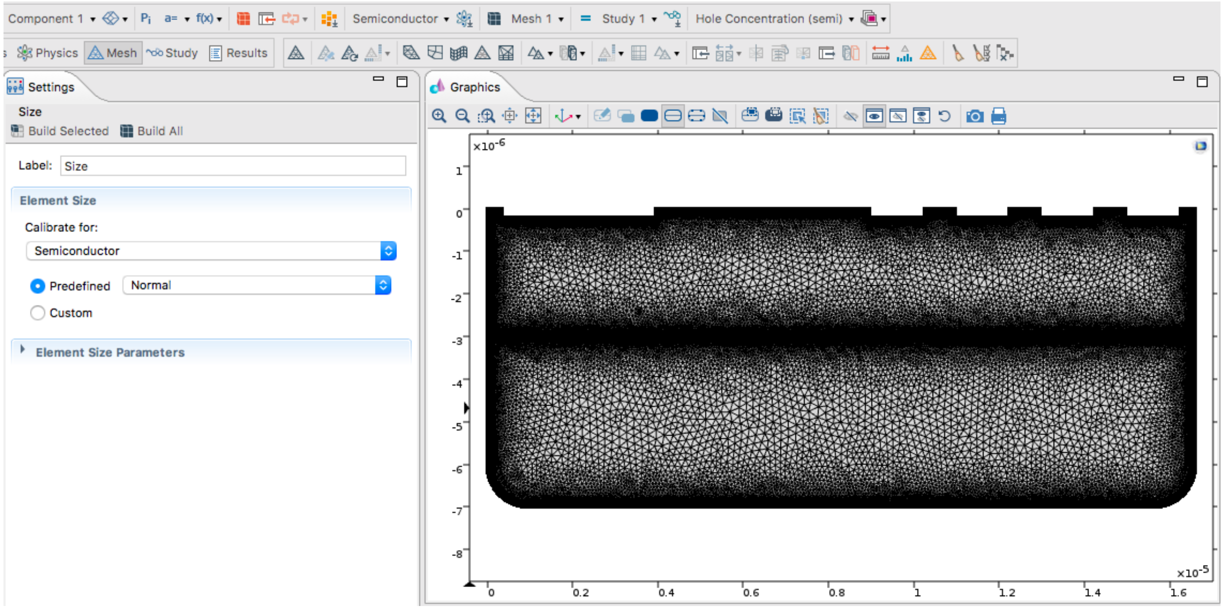

Size

Label: Size

Element Size

Calibrate for: Semiconductor

● Predefined Normal

○ Custom

Figure 6-3 The mesh for the WAS.

COMSOL^{TM} provides several *Study* modes, including stationary, time dependent, eigenfrequency, frequency domain, …etc. The time-independent continuity equation aims to find a solution to describe an equilibrium state. Therefore, the stationary study mode is the primary option.

COMSOL^{TM} also offers a useful function to sweep variable called the *Auxiliary Sweep*, as shown in red circle in Figure 6-4. In our project, the incident wavelength sweeps from 380 *n*m to 1000 *n*m. If more than two variables need to be swept, COMSOL^{TM} provides two sweep modes. The first mode is called *All Combinations*, which will solve for all combinations of variables, as its name indicates. The second mode is *Specified Combinations*, and it requires that each list of values have equal length. The first value in the first list only combines with the first value in the second list, and so on. Thus the total amount of combinations in this mode equals to the length of each list.

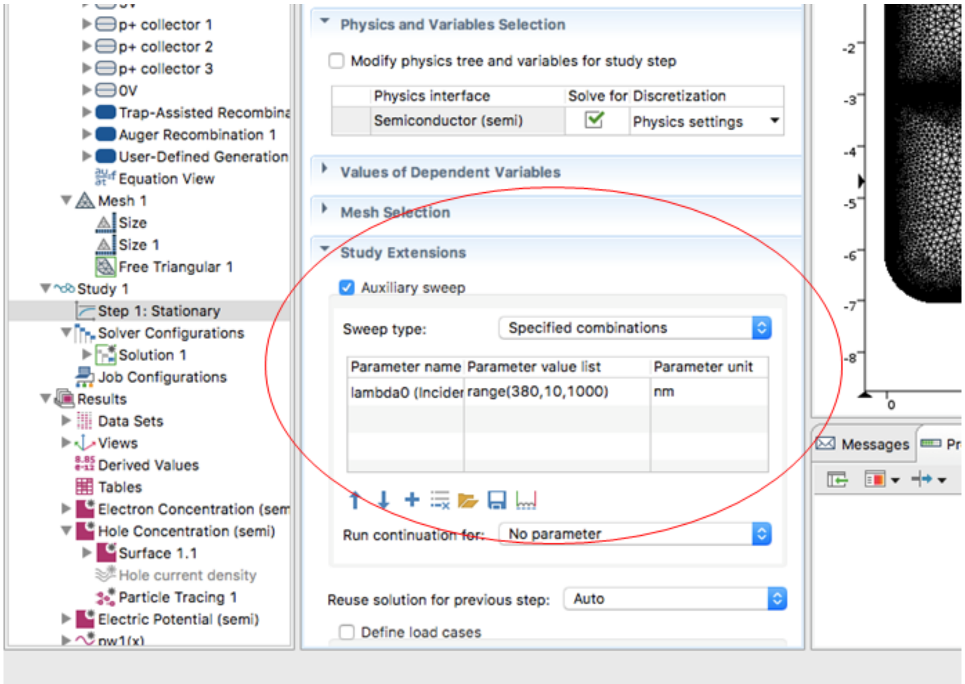

☐ Modify physics tree and variables for study step

Physics interface	Solve for	Discretization
Semiconductor (semi)	☑	Physics settings

☑ Auxiliary sweep

Sweep type: Specified combinations

Parameter name	Parameter value list	Parameter unit
lambda0 (Incider	range(380,10,1000)	nm

Run continuation for: No parameter

Reuse solution for previous step: Auto

☐ Define load cases

Figure 6-4 Stationary study mode and Auxiliary sweep function.

Now we present a short review on v3.5a. Since this version doesn’t provide the *Semiconductor* module, we use two type modules, *Electrostatics* and *Convection and Diffusion* modules, for electric field simulation and electron and holes transportation respectively, as seen in Figure 6-5. The *Electrostatics (init)* module gives the initial value of electric field as the first solution step, then other three modules, *Electrostatics (es)*, *Convection and Diffusion (cde)* for electrons, *Convection and Diffusion (cdh)* for holes, are coupled to solve the semiconductor model.

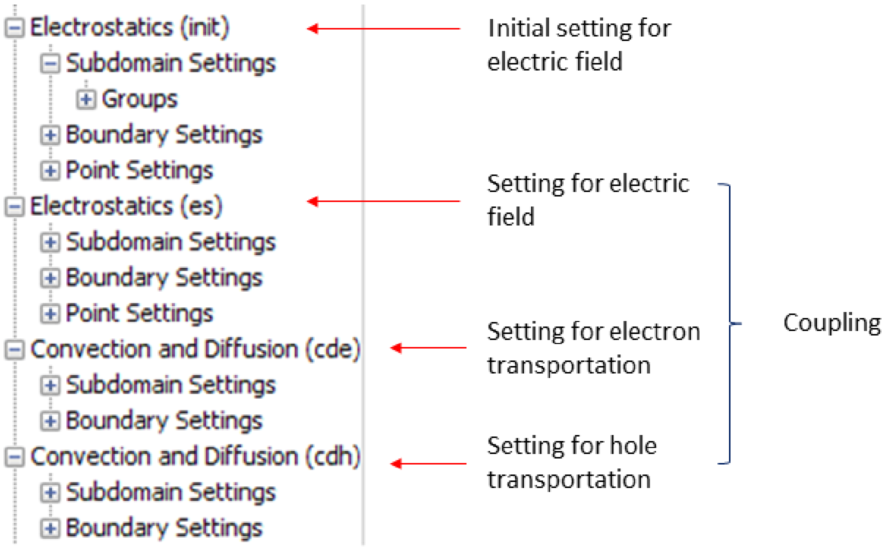

Figure 6-5 Modules in v3.5a for a semiconductor device simulation.

COMSOL^{TM} doesn't have a module to simulate Hall Effect. In v5.1, there is no option to add a magnetic field on a 2D model. In v3.5a, in the domain setting of *Convection and Diffusion* module, we can define mobility to induce the Hall Effect.

Mobility, μ, is a measure of the speed of an electron or a hole moving in a metal or a semiconductor, under an electric field [59]. Without a magnetic field, the hole velocity $\boldsymbol{v}$ is expressed as:

$$v_x = \mu_p E_x \, , v_y = \mu_p E_y \tag{6.1}$$

where μ_p is the hole mobility, E_x and E_y are the electric field in x and y direction (as shown in Figure 6-1). With magnetic field, holes are moving under the Lorentz force, and the current density $\boldsymbol{J}_p\,(\boldsymbol{B})$ obeys the equation:

$$\boldsymbol{J}_p\,(\boldsymbol{B}) = \boldsymbol{J}_p\,(0) + \mu_P\big(\boldsymbol{J}_{\boldsymbol{p}}\,(\boldsymbol{B}) \times \boldsymbol{B}\big) \tag{6.2}$$

where $\boldsymbol{J}_p\,(0)$ is the hole current density without the magnetic field, $\boldsymbol{J}_p\,(0) = q\mu_p\delta_p\boldsymbol{E} + qD_p\nabla\delta_p$. When $\boldsymbol{B}$ is perpendicular to $\boldsymbol{E}$, and the diffusion current density $qD_p\nabla\delta_p$ is negligible, then, Equation (6.2) becomes:

$$\boldsymbol{J}_p\,(\boldsymbol{B}) = \frac{q\mu_p\delta_p}{1+\mu_p^2B^2}[\boldsymbol{E} + \mu_p(\boldsymbol{B} \times \boldsymbol{E})] \tag{6.3}$$

In terms of $\boldsymbol{B} = (0, 0, -B_z)$, $\boldsymbol{E} = (E_x, E_y, 0)$, and $\boldsymbol{J}_p = q\delta_p\boldsymbol{v}$, the hole velocity becomes [49]:

$$v_x = \frac{\mu_p}{1+\mu_p^2B_z^2}\,(-E_x + \mu_n B_z E_y) \tag{6.4 (a)}$$

$$v_y = \frac{-\mu_p}{1+\mu_p^2B_z^2}\,(E_y + \mu_n B_z E_x) \tag{6.4 (b)}$$

The modified velocities setting containing the Hall Effect are marked in red circle in Figure 6-6.

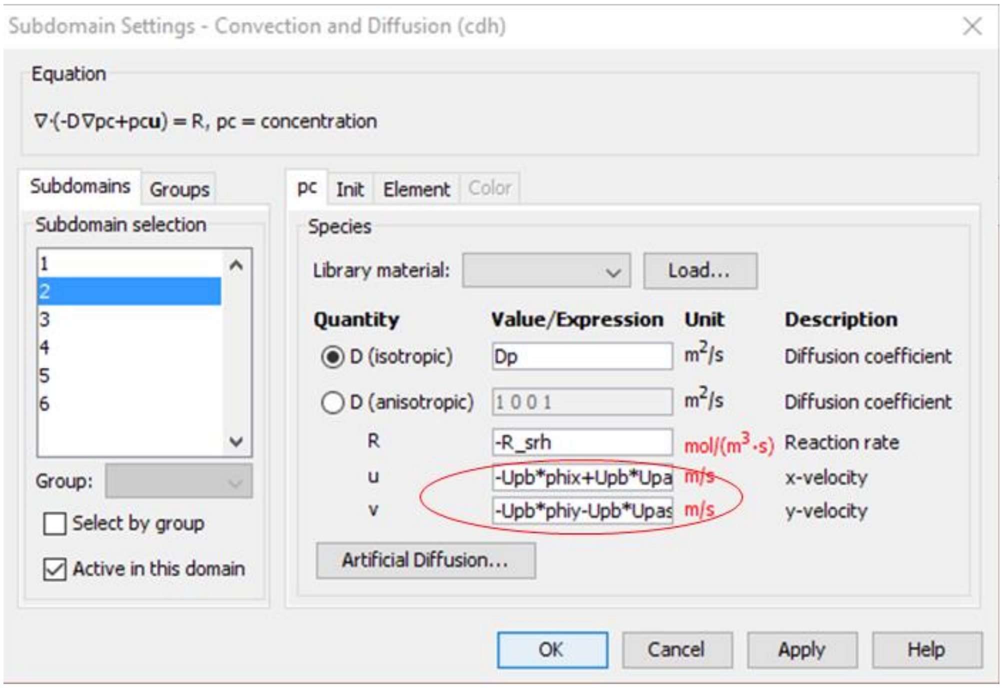

Equation

∇·(-D∇pc+pcu) = R, pc = concentration

☐ Select by group

☑ Active in this domain

Quantity	Value/Expression	Unit	Description
● D (isotropic)	Dp	m^2/s	Diffusion coefficient
○ D (anisotropic)	1 0 0 1	m^2/s	Diffusion coefficient
R	-R_srh	$mol/(m^3 \cdot s)$	Reaction rate
u	-Upb*phix+Upb*Upa	m/s	x-velocity
v	-Upb*phiy-Upb*Upas	m/s	y-velocity

Figure 6-6 Mobility definition for the Hall Effect.

6.2 Improved Models

The WAS prototype contains three collectors, as shown in Figure 3-1. The middle P+ collector collects holes, and a current is formed, which is used to make a spectrometer based on the equation:

$$J_B = M_{B\lambda}I_\lambda + J_{B,0} \tag{6.5}$$

$M_{B\lambda}$ is the $n\times n$ matrix of the J_B vs I_λ slopes for n magnetic fields and n wavelengths, and I_λ is the $n\times 1$ vector of the irradiances. For a 10×10 matrix, measurements of 10 irradiances for each of the 10 magnetic fields are required, thus a total of 100 slope values are achieved for calibration. Moreover, the generation of a magnetic field requires extra space. Eliminating the external magnet is necessary to realize a compact spectrometer or a spectral imager.

In this part, two improved models are proposed, as initial exploration on compact WAS without magnetic field. To obey the spectrometer principle, a few minor changes are made, in Section 6.2.1, more collectors are implanted to collect more data at once, and in Section 6.2.2, the depth of the left collector is changed to produce different current.

6.2.1 More P+ collectors

The first WAS prototype uses three collectors, and now more collectors are added as seen in Figure 6-7. As the same principle as of the first WAS, the collector 1 collects holes near the surface, collector 7 collects holes from deep range, and collector 2 to 6 collects holes from specific depths, respectively. Compared with the first prototype, the new structure can obtain five current points for an irradiance. For instance, with the new structure of pixel array shown in Figure 6-8, on a 20×20 pixel array, first four rows collect current from the collector 2, the next four rows use the collector 3, and so on, to end with the last four rows employing the collector 6.

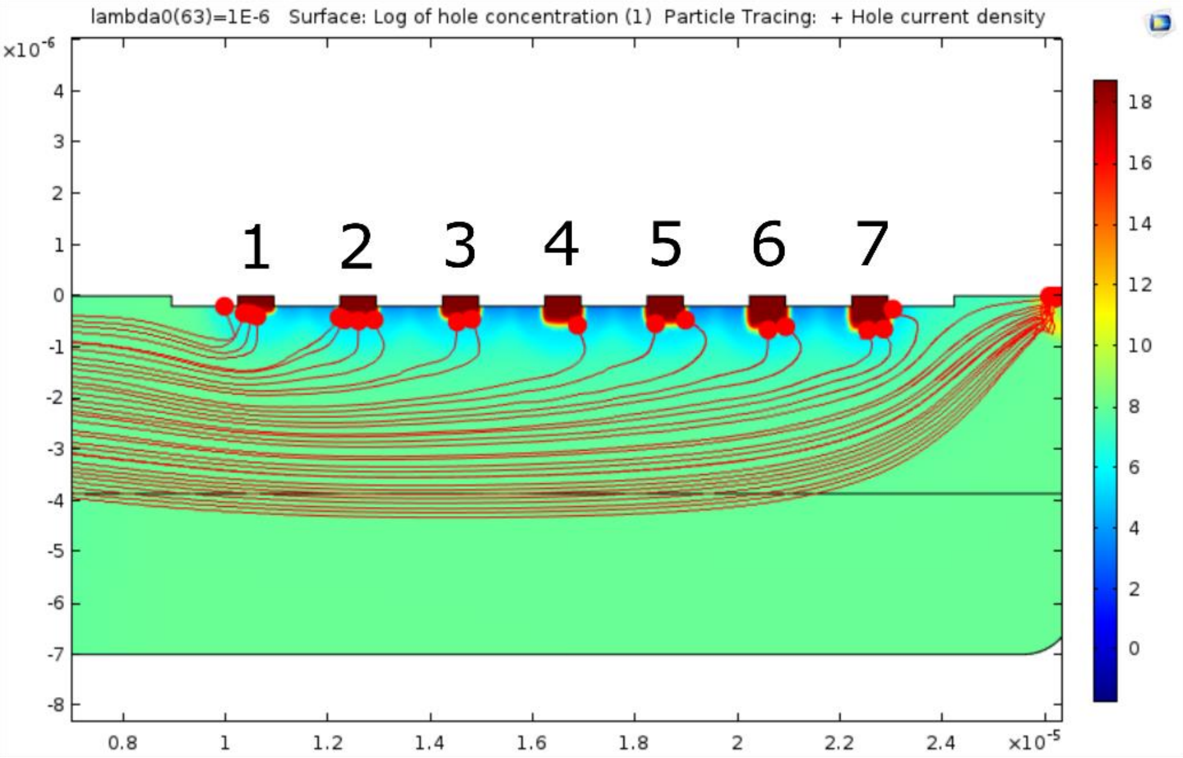

Figure 6-7 A sensor pixel with seven P+ collectors.

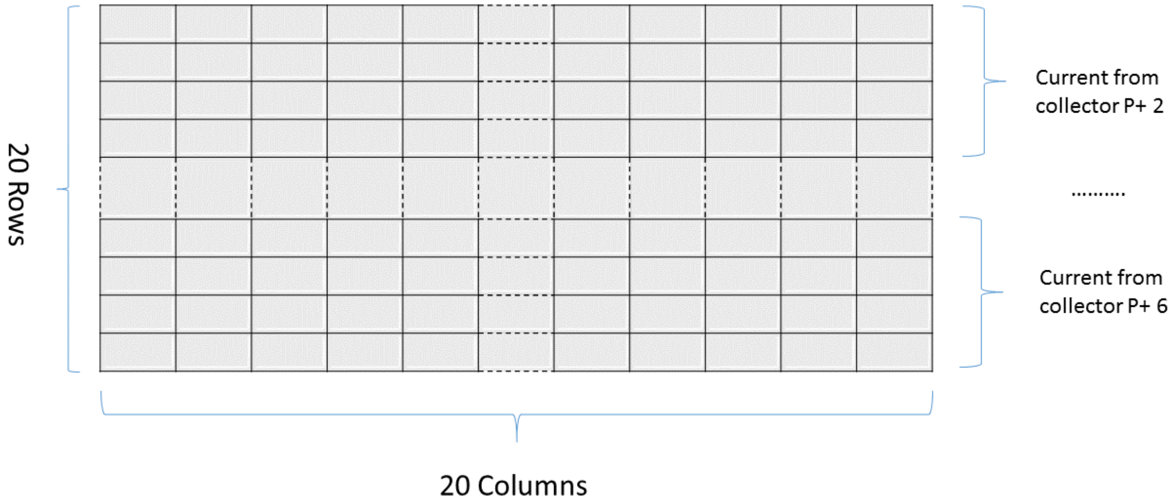

Figure 6-8 The new pixel array with the structure of Figure 6-7.

Figure 6-9 and Figure 6-10 give the simulation results of the current obtained from different collector vs incident wavelengths and incident irradiances respectively. As seen in Figure 6-10, the slope of the relationship is different for each collectors, making this novel structure ideal for a spectrometer application.

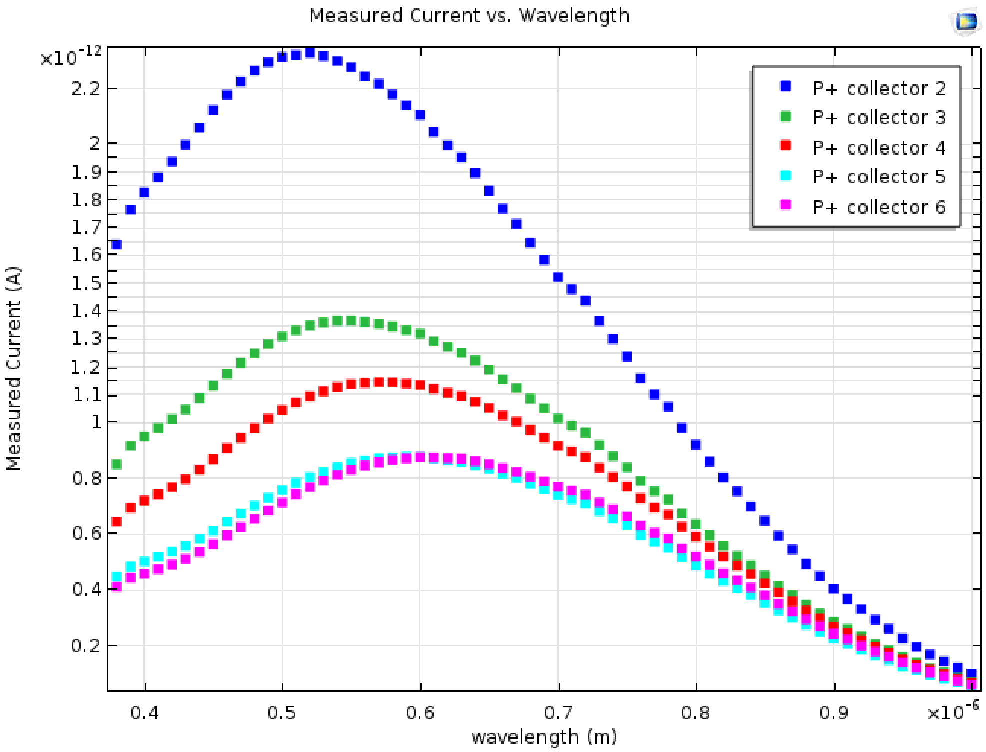

Figure 6-9 Current vs wavelength for several collectors.

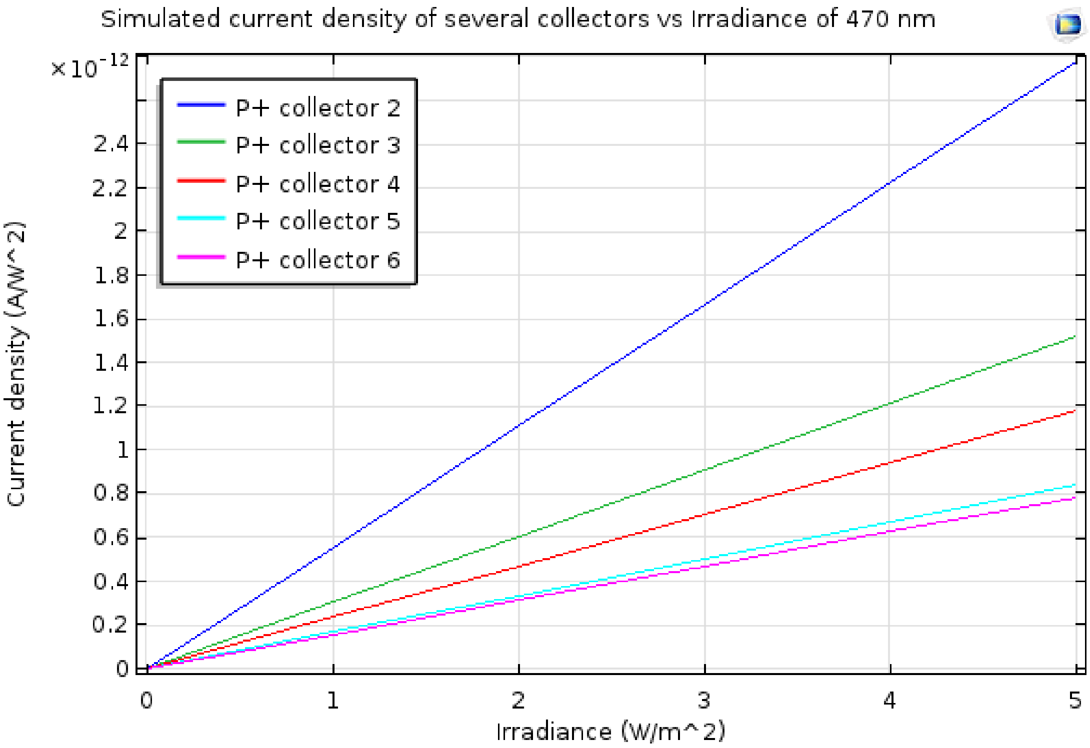

Figure 6-10 Current vs irradiance for several collectors.

The different collectors replace the need of a varying magnetic field on the structure presented in Chapter 3. Hence, Equation (3.19) can be written as:

$$J_i = M_{i\lambda} I_\lambda + J_{i,0} \tag{6.6}$$

i represents the collector number, $M_{i\lambda}$ is the $i \times i$ matrix of the current density vs irradiance slopes and I_λ is the $i \times 1$ vector of the irradiances. The matrix size is determined by the number of collectors. On the structure in Figure 6-7, i varies from 2 to 6, and the matrix size becomes 5×5.

A disadvantage of this structure is the low resolution due to the small number of collectors. A large number of collectors will produce a higher resolution, however, it will also reduce the response because the far collectors (such as collector 5 and 6 in Figure 6-9) have smaller and similar currents. On the other hand, the calibration procedure to obtain coefficients of the matrix $M_{i\lambda}$ is simplified.

6.2.2 The various depths of P1 collector

A similar idea to the previous design is proposed in this section. Multiple depths of a collector instead of multiple collectors are proposed in order to replace the effect of magnetic field.

As seen in Chapter 3, the P+ collectors shaped the electrical field around the collectors, and then determines the holes' current on the middle P+ collector. The left collector absorbs holes near the surface, and the range is determined by its depth. Changing the depth affects the holes' current collected by the middle collector. Figure 6-11 illustrates the several depths of the left collector, and Figure 6-12 provides the simulated current in the middle collector vs incident irradiances. The collector with large depth as seen in Figure 6-11 (c) results in smaller current because deeper left collector absorbs more holes, while small depth collector in Figure 6-11 (a) blocks fewer holes thus the current in the middle collector becomes larger.

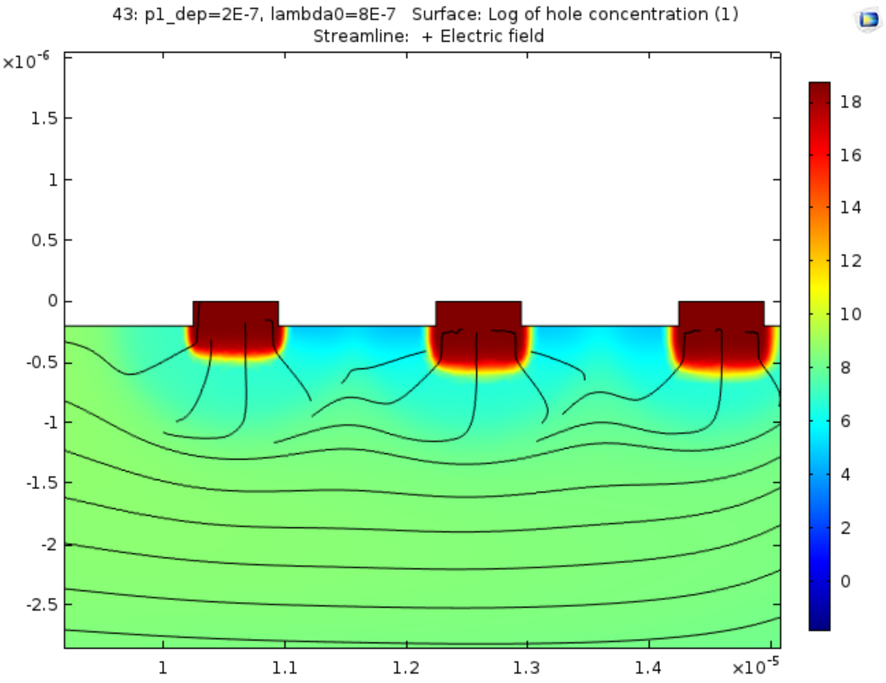

Figure 6-11 (a) The depth of left collector = 0.2 μm

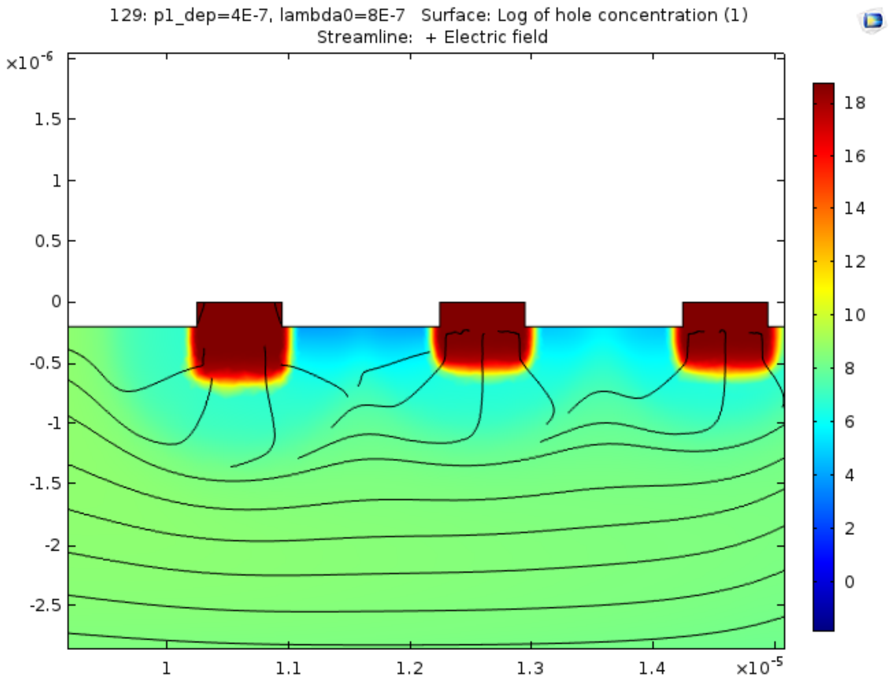

Figure 6-11 (b) The depth of left collector = 0.4 µm

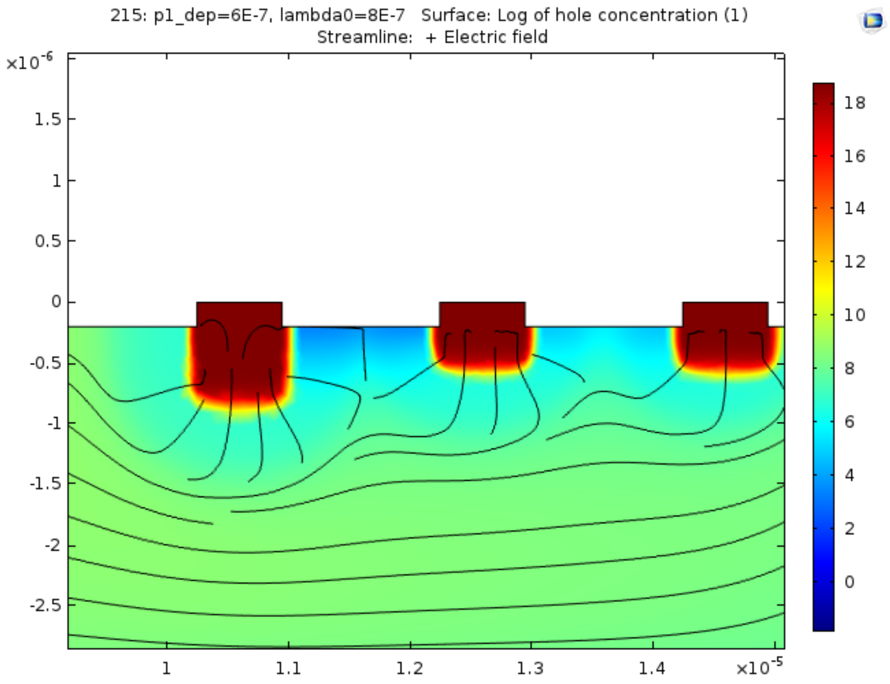

Figure 6-11 (c) The depth of left collector = 0.6 µm

Figure 6-11 COMSOL^{TM} modeled results for several depths of the left collectors.

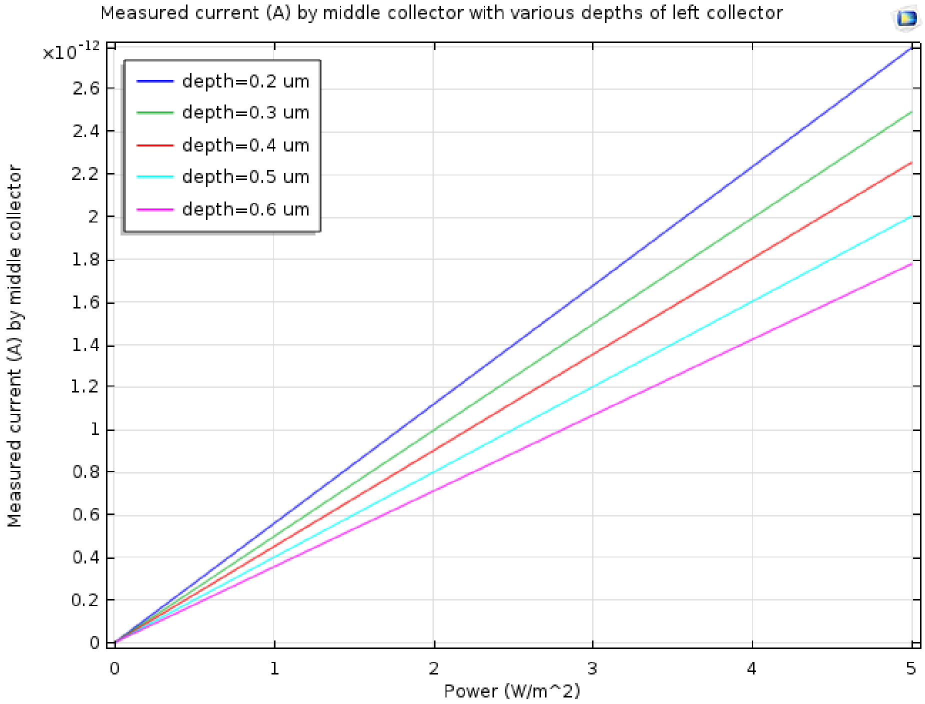

Figure 6-12 COMSOL^{TM} modeled current in the middle collector for different depths of the left collector.

Similar idea as section 6.2.1, a pixel array with five depths of the left collector can achieve five data at one measurement. Thus the Equation (3.19) becomes:

$$J_d = M_{d\lambda} I_\lambda + J_{d,0} \tag{6.7}$$

where, *d*, represents the variation depth of the left collector, $M_{d\lambda}$ is the $d \times d$ matrix of the current density vs irradiance slope and I_λ is the $d \times 1$ vector of the irradiances. The matrix size is determined by the number of depths. For the structure in Figure 6-11, *d* varies from 2 to 6, and the matrix becomes 5×5. This design has the same advantages and disadvantages as the previous one except that it could not be fabricated in a standard CMOS process given the lack of doping profile options.

6.3 Conclusion

In this chapter, we introduce the COMSOL model setup procedure on version 5.1, and then give simulation technique details of the Hall Effect on version 3.5a. In order to develop a compact spectrometer, two attempts are made to eliminate the need of space-consuming magnets. However, the low resolution is the main disadvantage of these modified pixel versions.

CHAPTER 7 CONCLUSION AND FUTURE WORK

7.1 Summary

This thesis proposes a novel micro-spectrometer without dispersing elements fabricated in standard CMOS technology. The spectrum detection principle is based on the wavelength absorption mechanism in silicon. Experimental results confirm the theoretical analysis proving that wavelength becomes indistinguishable at high concentration (>10^{16} cm^{-3}) since the Auger recombination mechanism is dominant. However, wavelength information can be obtained at low concentration when Shockley-Read-Hall (SRH) recombination mechanism prevails. A Finite Element Method model confirms the excess holes' detection principle as a function of depth where moving holes' trajectory is deviated under the Lorentz force towards a set of collectors. The developed light spectrum detection method require a linear equation set where coefficients of the matrix come from the measurement of the current density as a function of the irradiance for different wavelengths and magnetic fields.

Different from the traditional spectrometer, the resolution of the WAS depends on the minimal detectable current of excess holes. The theoretical calculation predicts that the resolution of the WAS could reach around 219 depending on the collectors' junction shot noise.

The continuity equation and the photo-generated excess carriers' concentration profile along depth (one-dimension) at equilibrium state are discussed in details. Boundary conditions, surface recombination velocity and carriers' lifetime are considered separately in order to explore their effects on the concentration profile. It was found that the surface recombination velocity doesn't have much effect while boundary conditions and carriers' lifetime have more impact.

In order to develop a compact spectrometer, two models are conceived where the detection principle does not rely on space-consuming magnets. However, the low resolution is the main disadvantage of these modified structures.

7.2 Contributions

The following main contributions have been achieved:

a) We have proposed the concept of spectrometry without dispersing element using a magnetic field. A monochrome light beam generates a unique excess carrier distribution along the incident depth due to the absorption coefficient. Hence, the wavelength information can be obtained by measuring the photo-generated carrier concentration as a function of depth under the Lorentz force.

b) We have validated the detection principle from solid-state physics analysis, finite element method model, and experimental results. Wavelength information could be obtained at low concentration when Shockley-Read-Hall (SRH) recombination mechanism prevails, while wavelength becomes indistinguishable at high concentration when the Auger recombination mechanism is dominant.

c) We have proposed two novel structures which eliminate the need of a magnetic field to obtain the coefficient matrix of the spectrometer.

7.3 Suggestions for future work

There are two suggestions for future work:

a) The resolution has reached the objective in a part range of the visible spectrum. More improvements on collectors' positions and the pixel geometry should be studied to increase the resolution in other spectrum range. Several groups of collectors, various positions of window area, and different N-well setting may have potential contributions.

b) The prototype WAS employs an external space-consuming magnetic field. Two improved models aiming to compact spectrometer without magnets have been proposed. However, they cannot achieve same-level resolution as the prototype WAS. Implanting more collectors is not an effective solution, and it will reduce the response as well. This is a challenge to explore a relationship between measured current and a physical quantity instead of the magnetic field to complete the calibration matrix.

BIBLIOGRAPHY

[1] D. J. Brady, *Optical Imaging and Spectroscopy*. John Wiley & Sons, 2009.

[2] J. M. Hollas, *Modern Spectroscopy*, 4th ed. John Wiley & Sons, Ltd, 2004.

[3] Y. Oike, M. Ikeda, and K. Asada, "A CMOS image sensor for high-speed active range finding using column-parallel time-domain ADC and position encoder," *Electron Devices IEEE Trans. On*, vol. 50, no. 1, pp. 152–158, 2003.

[4] W. W. Parson., *Modern Optical Spectroscopy*. Springer, 2007.

[5] J. Workman, "Optical Spectrometers," in *Applied Spectroscopy: A Compact Reference for Practitioners*, Academic Press, 1997, p. 3~28.

[6] B. Burke, P. Jorden, and P. Vu, "CCD Technology," *Exp. Astron.*, vol. 19, no. 1, pp. 69–102, 2005.

[7] Y. Tetsuo, "CCD Image Sensors," in *Image Sensors and Signal Processing for Digital Still Cameras*, 0 vols., CRC Press, 2005, pp. 95–141.

[8] M. Bigas, E. Cabruja, J. Forest, and J. Salvi, "Review of CMOS image sensors," *Microelectron. J.*, vol. 37, no. 5, pp. 433–451, 2006.

[9] G. de Graaf and R. F. Wolffenbuttel, "Optical CMOS sensor system for detection of light sources," *Sens. Actuators Phys.*, vol. 110, no. 1–3, pp. 77–81, Feb. 1, 2004.

[10] A. Hoffman, M. Loose, and V. Suntharalingam, "CMOS Detector Technology," *Exp. Astron.*, vol. 19, no. 1, pp. 111–134, 2005.

[11] T. Isao, "CMOS Image Sensors," in *Image Sensors and Signal Processing for Digital Still Cameras*, 0 vols., CRC Press, 2005, pp. 143–178.

[12] J. Ohta, "Fundamentals of CMOS image sensors," in *Smart CMOS Image Sensors and Applications*, 0 vols., CRC Press, 2007, pp. 11–57.

[13] S. A. Taylor, "CCD and CMOS Imaging Array Technologies: Technology Review." Citeseer, 1998.

[14] O. Vellacott, "CMOS in camera," *IEE Rev.*, vol. 40, no. 3, pp. 111–114, 1994.

[15] Y. Wang, S. Barna, S. Campbell, and E. R. Fossum, "A high dynamic range CMOS APS image sensor," in *IEEE Workshop CCD and Advanced Image Sensors, Lake Tahoe, Nevada, USA*, 2001.

[16] G. Q. Zhang *et al.*, "Semiconductor Image Sensing," in *More than Moore*, Springer US, 2009, pp. 239–278.

[17] I. RUSH A (Foveon California) HUBEL P.(Foveon, Inc. ..California), "X3 Sensor Characteristics," *J. Soc. Photogr. Sci. Technol. Jpn.*, vol. 66, 2003.

[18] Y. Audet, "A filterless color image sensor for digital camera," PCT/CA2007/000997, 2007.

[19] Sze, *Physics of Semiconductor Devices*, 3rd ed. 2007.

[20] D. K. Schroder, *Semiconductor Material and Device Characterization*, 2nd ed. New York: John Wiley & Sons, 1998.

[21] E. R. Fossum, "CMOS image sensors: electronic camera-on-a-chip," *Electron Devices IEEE Trans. On*, vol. 44, no. 10, pp. 1689–1698, 1997.

[22] C. C. Wang, "A study of CMOS technologies for image sensor applications." Citeseer, 2001.

[23] B. D. Bartolo and J. Collins, "LUMINESCENCE SPECTROSCOPY Handbook of Applied Solid State Spectroscopy," D. R. Vij, Ed. Springer US, 2006, pp. 509–575.

[24] "Why is diffraction grating more accurate than double slits to measure the wavelength of light? | Socratic," *Socratic.org*. [Online]. Available: https://socratic.org/questions/why-is-diffraction-grating-more-accurate-than-double-slits-to-measure-the-wavele [Accessed: 13-Sep-2017].

[25] Krishnavedala, *By Krishnavedala - Own work, CC BY-SA 4.0, https://commons.wikimedia.org/w/index.php?curid=36946699*

[26] "By Stigmatella_aurantiaca (talk) (Uploads)File 1: FL0 at de.wikipediaFile 2: Epzcaw - A composite image of my own work, created in Inkscape, :File:Interferenz-michelson.jpg, created by FL0 at de.wikipedia and licensed under CC-BY-SA-3.0; CC-BY-SA-3.0-DE; BILD-GFDL-NEU, and :File:SodiumD two double slits 2.jpg uploaded by Epzcaw and licensed under Creative Commons Attribution-Share Alike 3.0 Unported license., CC BY-SA 3.0, https://commons.wikimedia.org/w/index.php?curid=20108988" *Wikipedia*. 02-May-2017.

[27] B. E. Bayer, "Color Imaging Array," US3971065 A, 20-Jul-1976.

[28] R. B. (Woodside Merrill CA), "Color separation in an active pixel cell imaging array using a triple-well structure," US5965875, 12-Oct-1999.

[29] "FOVEON X3 14.1 MP." [Online]. Available: http://www.foveon.com/article.php?a=222

[30] G. Langfelder, A. Longoni, and F. Zaraga, "The Transverse Field Detector: a CMOS active pixel sensor capable of on-line tuning of the spectral response," in *2009 IEEE Sensors*, 2009, pp. 1652–1657.

[31] Y. Maruyama, K. Sawada, H. Takao, and M. Ishida, “The fabrication of filter-less fluorescence detection sensor array using CMOS image sensor technique,” *Sens. Actuators Phys.*, vol. 128, no. 1, pp. 66–70, Mar. 2006.

[32] H. Nakazawa, K. Yamasaki, K. Takahashi, M. Ishida, and K. Sawada, “A filter - less multi - wavelength fluorescence detector,” in *2011 16th International Solid-State Sensors, Actuators and Microsystems Conference*, 2011, pp. 100–103.

[33] K. Tanaka, Y. Kimura, Y. J. Choi, T. Iwata, K. Takahashi, and K. Sawada, “Realization of filter-free fluorescence image sensor,” in *2017 19th International Conference on Solid-State Sensors, Actuators and Microsystems (TRANSDUCERS)*, 2017, pp. 1616–1619.

[34] “Mini-spectrometers | Hamamatsu Photonics.” [Online]. Available: http://www.hamamatsu.com/us/en/product/category/5001/4016/index.html [Accessed: 06-Apr-2017].

[35] “Ocean Optics Spectrometers | Cuvettes | O2 Sensors,” *Spectrecology - Spectroscopy & Optical Sensing Solutions*. [Online]. Available: http://www.spectrecology.com/ [Accessed: 06-Apr-2017].

[36] “Spectrometers | LightMachinery.” [Online]. Available: https://lightmachinery.com/hyperfine-spectrometer/ [Accessed: 06-Apr-2017].

[37] “Spectrometers - Spectral Products.” [Online]. Available: http://www.spectralproducts.com/spectrometers.html [Accessed: 06-Apr-2017].

[38] M. Muneeb *et al.*, “III-V-on-silicon integrated micro - spectrometer for the 3 μm wavelength range,” *Opt. Express*, vol. 24, no. 9, pp. 9465–9472, May 2016.

[39] P. Pottier, M. J. Strain, and M. Packirisamy, “Integrated Microspectrometer with Elliptical Bragg Mirror Enhanced Diffraction Grating on Silicon on Insulator,” *ACS Photonics*, vol. 1, no. 5, pp. 430–436, May 2014.

[40] Feng Zheng, Liying Liu, Guoyu Zhang, Kewei Huan, Ye Li, and Xiaoguang Shi, “Compact spectrometer based on concave grating,” 2015, vol. 9795, p. 97951C–9795–4.

[41] A. Y. Zhu *et al.*, “Compact hyper-spectrometer based on metasurfaces at visible wavelengths,” in *Frontiers in Optics 2016 (2016), paper JW4A.65*, 2016, p. JW4A.65.

[42] J. A. Carlson *et al.*, “Integration of linear variable filters on CMOS for compact emission and absorption sensing,” in *2016 IEEE SENSORS*, 2016, pp. 1–3.

[43] M. Yang, H. Wang, M. Li, and J.-J. He, “An echelle diffraction grating for imaging spectrometer,” presented at the Infrared Remote Sensing and Instrumentation XXIV, 2016, vol. 9973, p. 99730D.

[44] Z. Xu, Z. Wang, M. E. Sullivan, D. J. Brady, S. H. Foulger, and A. Adibi, “Multimodal multiplex spectroscopy using photonic crystals,” *Opt. Express*, vol. 11, no. 18, pp. 2126–2133, Sep. 2003.

[45] G. Schweiger, R. Nett, and T. Weigel, “Microresonator array for high-resolution spectroscopy,” *Opt. Lett.*, vol. 32, no. 18, pp. 2644–2646, Sep. 2007.

[46] “COMSOL Multiphysics® Modeling Software.” [Online]. Available: https://www.comsol.com/ [Accessed: 02-May-2017].

[47] S. K. B. B. J. Streetman, *Solid State Electronic Devices*, 6th ed. Pearson Prentice Hall, 2006.

[48] B. Lojek, “Reflectivity of the silicon semiconductor substrate and its dependence on the doping concentration and intensity of the irradiation,” in *11th IEEE International Conference on Advanced Thermal Processing of Semiconductors. RTP 2003*, 2003, pp. 215–220.

[49] H. P. Baltes and R. S. Popovic, “Integrated semiconductor magnetic field sensors,” *Proc. IEEE*, vol. 74, no. 8, pp. 1107–1132, 1986.

[50] T. H. Lee, *The Design of CMOS Radio-Frequency Integrated Circuits*. Cambridge University Press, 2003.

[51] W. D. Eades and R. M. Swanson, “Calculation of surface generation and recombination velocities at the Si-SiO2 interface,” *J. Appl. Phys.*, vol. 58, no. 11, pp. 4267–4276, 1985.

[52] D. K. Schroder, “Carrier lifetimes in silicon,” *Electron Devices IEEE Trans. On*, vol. 44, no. 1, pp. 160–170, 1997.

[53] D. K. Schroder *et al.*, “Silicon epitaxial layer recombination and generation lifetime characterization,” *Electron Devices IEEE Trans. On*, vol. 50, no. 4, pp. 906–912, 2003.

[54] R. A. Sinton and A. Cuevas, “Contactless determination of current–voltage characteristics and minority-carrier lifetimes in semiconductors from quasi-steady-state photoconductance data,” *Appl. Phys. Lett.*, vol. 69, no. 17, pp. 2510–2512, Oct. 1996.

[55] D. J. Roulston, N. D. Arora, and S. G. Chamberlain, “Modeling and measurement of minority-carrier lifetime versus doping in diffused layers of n+-p silicon diodes,” *IEEE Trans. Electron Devices*, vol. 29, no. 2, pp. 284–291, Feb. 1982.

[56] F. P. Heiman, “On the determination of minority carrier lifetime from the transient response of an MOS capacitor,” *Electron Devices IEEE Trans. On*, vol. 14, no. 11, pp. 781–784, 1967.

[57] T. J. R. Hughes, *The Finite Element Method: Linear Static and Dynamic Finite Element Analysis*. Courier Corporation, 2012.

[58] N. S. Ottosen and H. Petersson, *Introduction to the Finite Element Method*. Prentice-Hall, 1992.

[59] P. D. P. Y. Yu, P. Dr, and D. h c M. Cardona, “Electrical Transport,” in *Fundamentals of Semiconductors*, Springer Berlin Heidelberg, 2010, pp. 203–241.

APPENDIX A – VHDL CODE

VHDL code of selecting signals

```
-- GRM, Polytechnique de Montreal
-- Author: Kai Zhang


-- Create Date:  2014/02/12
-- Target Device: Actel A40MX04PL84



----------------------------------------------
library IEEE;
use IEEE.STD_LOGIC_1164.ALL;
use IEEE.STD_LOGIC_ARITH.ALL;
use IEEE.STD_LOGIC_UNSIGNED.ALL;
----------------------------------------------------
Entity FPGA42MX is
port (
    clk, scan_mode, row_sel, reset: IN STD_LOGIC;
    clk_pixel: out std_logic;
         Csync, Rsync: out std_logic;
         Column: out std_logic_vector(19 downto 0);
         Row: out std_logic_vector(19 downto 0)
         );
end FPGA42MX;
```

```
------------------------------------------------------------
Architecture Code of FPGA42MX is


-- internal signals between three blocks
signal clk_col: std_logic := '0';--initial values for simulation
signal clk_row: std_logic := '0';--initial values for simulation


-- internal signals in freq_divider 1
signal countQ: std_logic_vector(3 downto 0) := "0000";


-- internal signals in col
signal countC: std_logic_vector(4 downto 0) := "00000";


-- internal signals in freq_divider 2 and row
signal countQ2: std_logic_vector(3 downto 0) := "0000";
signal countR: std_logic_vector(4 downto 0) := "00000";


begin
------------------------------------------------------------------
proc_freq_divider1: -- ten times divider
process (reset, clk)
begin
        if (reset='1') then                 --reset all
                clk_col <= '0';
```

```
                countQ <= "0000";


        else

                if(clk'event and clk = '1') then

                --ten times divider

                        if(countQ /= 4) then

                        countQ <= countQ + 1;

                        else

                        clk_col <= not clk_col;

                        CountQ <= (others =>'0');

                        end if;

                end if;

        end if;


end process proc_freq_divider1;


------------------------------------------------------------------

proc_freq_divider2: -- 20 times divider of clk_col

process (reset, clk_col)

begin

        if (reset='1') then                     --reset all

                clk_row <= '0';

                countQ2 <= "0000";
```

```
          else
                    if(clk_col'event and clk_col = '1') then
                    -- 20 times frequency divider of clk_col
                              if(countQ2 /= 9) then
                                        CountQ2 <= CountQ2 + 1;
                              else
                                        clk_row <= not clk_row;
                                        CountQ2 <= (others =>'0');
                              end if;
                    end if;
          end if;
end process proc_freq_divider2;
----------------------------------------------
proc_col_auto_scan:
process (reset, clk_col)
begin
          if (reset='1') then                             -- reset
                    Csync <= '0';
                    countC <= "00000";
                    Column <= "00000000000000000000";
          elsif (rising_edge(clk_col)) then
                    Csync <= '1';
                    countC <= countC+1;
                                        if(countC="10100") then
```

```
        countC <= "00000";
        end if;
        case countC is

when "00001" => Column <= "00000000000000000001";
when "00010" => Column <= "00000000000000000010";
when "00011" => Column <= "00000000000000000100";
when "00100" => Column <= "00000000000000001000";
when "00101" => Column <= "00000000000000010000";

when "00110" => Column <= "00000000000000100000";
when "00111" => Column <= "00000000000001000000";
when "01000" => Column <= "00000000000010000000";
when "01001" => Column <=  "00000000000100000000";
when "01010" => Column <= "00000000001000000000";

when "01011" => Column <= "00000000010000000000";
when "01100" => Column <= "00000000100000000000";
when "01101" => Column <= "00000001000000000000";
when "01110" => Column <= "00000010000000000000";
when "01111" => Column <= "00000100000000000000";

when "10000" => Column <= "00001000000000000000";
when "10001" => Column <= "00010000000000000000";
```

```
                when "10010" => Column <= "00100000000000000000";
                when "10011" => Column <= "01000000000000000000";
                when "10100" => Column <= "10000000000000000000";

                when others => Column <= "00000000000000000000";
                end case;
    end if;
end process proc_col_auto_scan;
----------------------------------------------------------------------
proc_freq_divider2_row_sel:  -- row scan auto/manual
process (reset, row_sel, clk_row, scan_mode)
begin
    if (reset='1') then                             -- reset
        Rsync <= '0';
        countR <= "00000";
        Row <= "11111111111111111111";
    elsif(clk_row='1' and clk_row'event) then -- auto scan
                if (scan_mode ='1') then -- row circle auto
                countR <= countR+1;
                Rsync <= '1';
                if(countR="10100") then
                        countR <= "00000";
                    end if;
                case countR is
```

```
when "00001" => Row <= "11111111111111111110";
when "00010" => Row <= "11111111111111111101";
when "00011" => Row <= "11111111111111111011";
when "00100" => Row <= "11111111111111110111";
when "00101" => Row <= "11111111111111101111";

when "00110" => Row <= "11111111111111011111";
when "00111" => Row <= "11111111111110111111";
when "01000" => Row <= "11111111111101111111";
when "01001" => Row <= "11111111111011111111";
when "01010" => Row <= "11111111110111111111";

when "01011" => Row <= "11111111101111111111";
when "01100" => Row <= "11111111011111111111";
when "01101" => Row <= "11111110111111111111";
when "01110" => Row <= "11111101111111111111";
when "01111" => Row <= "11111011111111111111";

when "10000" => Row <= "11110111111111111111";
when "10001" => Row <= "11101111111111111111";
when "10010" => Row <= "11011111111111111111";
when "10011" => Row <= "10111111111111111111";
when "10100" => Row <= "01111111111111111111";
```

```
when others => Row <= "11111111111111111111";
end case;                         -- row output, circle mode


elsif(scan_mode='0' and row_sel='1') then
countR <= countR+1;
Rsync <= '1';
if(countR="10100") then
                countR <= "00000";
        end if;
case countR is
when "00001" => Row <= "11111111111111111110";
when "00010" => Row <= "11111111111111111101";
when "00011" => Row <= "11111111111111111011";
when "00100" => Row <= "11111111111111110111";
when "00101" => Row <= "11111111111111101111";


when "00110" => Row <= "11111111111111011111";
when "00111" => Row <= "11111111111110111111";
when "01000" => Row <= "11111111111101111111";
when "01001" => Row <= "11111111111011111111";
when "01010" => Row <= "11111111110111111111";


when "01011" => Row <= "11111111101111111111";
when "01100" => Row <= "11111111011111111111";
```

```
                when "01101" => Row <= "11111110111111111111";
                when "01110" => Row <= "11111101111111111111";
                when "01111" => Row <= "11111011111111111111";

                when "10000" => Row <= "11110111111111111111";
                when "10001" => Row <= "11101111111111111111";
                when "10010" => Row <= "11011111111111111111";
                when "10011" => Row <= "10111111111111111111";
                when "10100" => Row <= "01111111111111111111";

                when others => Row <= "11111111111111111111";
                end case;               -- row output, circle mode
                end if;
        end if;

end process proc_freq_divider2_row_sel;
------------------------------------------------
clk_pixel <= clk;
------------------------------------------------
end Code;
```

APPENDIX B – RESOLUTION CALCULATION CODE

Resolution calculation code by MATLAB.

```
-------------------------------------------------

% to calculate the resolution of the spectrometer
% R= excess holes/delta excess holes
% calculate the R, the target wavelength is
% the middle wavelength for each delta_lambda


clf;
close all;
clear;
format short eng; % display 5 digits and 3 index


q = 1.6e-19; % unit C. electron
Power=4; %unit W/m^2;
h= 6.63*10^(-34); %unit J*s
c=3*10^8; %unit m/s
color=['b','c','g','r','y','m','r','k','b','c','g','y','m','r','k'];
i=1;
delta_w_max = -80;
step = -1;
delta_holes = sqrt(2*q*5e-12*10e6)/(q*200*3.41e-8);
i_noise = sqrt(2*q*5e-12*10e6); % noise current
resolution = zeros(1000,3); % to save the data of delta_holes vs delta_w
```

```
del_w = zeros(delta_w_max/step,1); % record the delta_w

del_hole = zeros(delta_w_max/step,1); % record the delta_holes

del_hole_2 = zeros(delta_w_max/step,1); % record the delta_holes_2

alpha = zeros(1000,2); % to record the absorption coeff.

k=0; % to record the resolution vs wave.

%%

for w=400:1:800; % set the zero point of wavelength   NEED INPUT **


   y = 0.9e-4; % 1/alpha_approx(w); % cm

   y1=y-0.1*10^(-4); % upper boundary

   y2=y+0.1*10^(-4); % lower boundary

   j=1; % used when save data to Cross

   a1=alpha_approx(w);  % input nm, output cm

   alpha(i,1) = w;

   alpha(i,2) = a1;

   I1 = 1e-13*Power*w/(h*c); % unit 1/cm2s

   f1=@(y) (a1*I1*exp(-a1*abs(y)));  % unit 1/cm3s

   holes1 = integral(f1,y1,y2); % excess holes unit 1/cm2s


   for delta_w = step:step:delta_w_max; % scan parameter


      del_w(j) = delta_w;

      w2= w+delta_w;

      a2=alpha_approx(w2);
```

```
I2 = 1e-13*Power*w2/(h*c); % unit 1/cm2s
f2=@(y) (a2*I2*exp(-a2*abs(y)));  % unit 1/cm3s
holes2 = integral(f2,y1,y2); % excess holes unit 1/cm2s
del_hole(j) = abs(holes1-holes2);
figure(1);
plot(delta_w,(abs(holes1-holes2)),'r*','markersize',1);
plot(delta_w,(delta_holes),'k.','markersize',4);
hold on;
if j>1
    if del_hole(j)>delta_holes &&  del_hole(j-1)<delta_holes
      % slope = (del_hole(j)-del_hole(j-1))/step;
      % A = del_hole(j)-del_hole(j-1)-slope*delta_w; % intersection
       delta_w_cross = delta_w-step;  % position x value. not accurate, very close
      % delta_w_cross = (delta_holes-A)/slope  % position x value
       k=k+1;
       resolution(k,1)=w;
       resolution(k,2)=delta_w_cross;
       figure(2);
        plot(w,abs(delta_w_cross),'r*','markersize',6);
        hold on;
       figure(3);
        plot(w,abs(w/delta_w_cross),'r*','markersize',6);
        hold on;
    else
```

```
         end
      else
      end
      j=j+1;
   end
   i=i+1;
end
figure(1);
xlabel('Resolving Power (nm)','fontsize',12);
ylabel('hole-delta-concentration (1/cm^3)','fontsize',12);
title('Resolving Power in the visible range','fontsize',12);
figure(2);
xlabel('Wavelength (nm)','fontsize',12);
ylabel('Resolving Power (nm)','fontsize',12);
title('Resolving Power vs. Wavelength','fontsize',12);
figure(3);
xlabel('Wavelength (nm)','fontsize',12);
ylabel('Resolution','fontsize',12);
title('Resolution vs. Wavelength','fontsize',12);
```